



# Porosity-driven convection and asymmetry beneath mid-ocean ridges

Richard F. Katz

*Department of Earth Sciences, University of Oxford, South Parks Road, Oxford OX1 3AN, UK  
(richard.katz@earth.ox.ac.uk)*

[1] Seismic tomography of the asthenosphere beneath mid-ocean ridges has produced images of wave speed and anisotropy that are asymmetric across the ridge axis. These features have been interpreted as resulting from an asymmetric distribution of upwelling and melting. Using computational models of coupled magma/mantle dynamics beneath mid-ocean ridges, I show that such asymmetry should be expected if buoyancy forces contribute to mantle upwelling beneath ridges. The sole source of buoyancy considered here is the dynamic retention of less dense magma within the pores of the mantle matrix. Through a scaling analysis and comparison with a suite of simulations, I derive a quantitative prediction of the contribution of such buoyancy to upwelling; this prediction of convective vigor is based on parameters that, for the Earth, can be constrained through natural observations and experiments. I show how the width of the melting region and the crustal thickness, as well as the susceptibility to asymmetric upwelling, are related to convective vigor. I consider three causes of symmetry breaking: gradients in mantle potential temperature and composition and ridge migration. I also report that in numerical experiments performed for this study, the fluid dynamical instability associated with porosity/shear band formation is not observed to occur.

**Components:** 20,100 words, 13 figures, 3 tables.

**Keywords:** mid-ocean ridge; convection; magma; plate tectonics; active flow; volcanism.

**Index Terms:** 8120 Tectonophysics: Dynamics of lithosphere and mantle: general (1213); 8121 Tectonophysics: Dynamics: convection currents, and mantle plumes; 1037 Geochemistry: Magma genesis and partial melting (3619).

**Received** 1 July 2010; **Revised** 21 September 2010; **Accepted** 23 September 2010; **Published** 10 November 2010.

Katz, R. F. (2010), Porosity-driven convection and asymmetry beneath mid-ocean ridges, *Geochem. Geophys. Geosyst.*, *11*, Q0AC07, doi:10.1029/2010GC003282.

**Theme:** Geochemical Heterogeneities in Oceanic Island Basalt and Mid-ocean Ridge  
Basalt Sources: Implications for Melting Processes and Mantle Dynamics

**Guest Editors:** C. Beier and P. Asimow

## 1. Introduction

[2] The global mid-ocean ridge (MOR) system is greater than 50,000 km in length and spans all of the ocean basins on the planet [Ito and Dunn, 2009]. Physical and chemical properties of the ridge axis, and their geographical variation, provide fundamental constraints on the dynamics and petrology of

the otherwise inaccessible mantle below. A primary variable in the geographical diversity of the ridge system is the rate of divergence of adjacent plates; the full-spreading rate varies from ultraslow (~1 cm/yr) to fast (~15 cm/yr). It has long been a goal of MOR studies to correlate the spreading rate with other features that are observed to vary geographically. These efforts have met with partial success [e.g.,

*Bown and White, 1994*], but it is clear that much of the diversity of the ridge system cannot be explained by spreading rate alone [e.g., *Small, 1994; Rubin and Sinton, 2007*]. Mantle heterogeneity must play a role too, and *Langmuir et al. [1992]* have shown that geographic variation in mantle potential temperature can account for significant differences between segments of the ridge. Despite such progress, and despite the simplicity of MOR volcanism relative to other volcanic settings, many observations of MORs remain unexplained. These observations may help us to refine models of the fluid dynamics and petrology of the asthenosphere beneath ridges.

[3] Past work on subridge mantle dynamics has focused on two basic models: passive and active flow. Passive mantle flow is driven by external forcing, imposed as boundary conditions on models. Tectonic plate divergence is the primary example of such forcing, and when applied as a boundary condition to viscous flow models of mantle dynamics, it gives rise to upwelling flow that turns a corner and moves laterally away from the ridge axis [*Batchelor, 1967; McKenzie, 1969; Lachenbruch, 1976*]. In contrast, active flow is calculated by accounting for buoyancy forces as well as boundary conditions. In a model that accounts for buoyancy, density gradients can give rise to time-dependent, convective flows that are not present in passive models. Previous authors have argued that the effects of active flow are absent from MOR data, and therefore the passive model (i.e., neglecting buoyancy forces) is appropriate [e.g., *Spiegelman and Reynolds, 1999*]. The purpose of the present work is to reconsider the effects of buoyancy on MOR dynamics, and show that it may help to explain the asymmetric distribution of melt observed in the subridge mantle by seismic tomography.

[4] Because most magma produced in the MOR environment is focused to the ridge axis, the spatial distribution of mantle melting cannot typically be inferred from petrologic observations. Hence petrologic studies of mid-ocean ridge basalt (MORB) formation [e.g., *McKenzie and Bickle, 1988; Langmuir et al., 1992*] have tended to favor the simpler theory of passive flow of the mantle beneath ridges. Petrology tells us that melting occurs in the region where the mantle is upwelling at temperatures above the mantle solidus. For passive flow, this region is found to be approximately triangular in cross section; it is centered beneath the ridge axis and symmetric across it.

[5] Observations of the mantle asthenosphere made with seismic tomography are a challenge to this

simple picture of symmetric, plate-driven flow. Tomographic studies exploit the sensitivity of seismic wave speed to the presence of magma at mantle grain boundaries [e.g., *Blackman and Kendall, 1997; Yang et al., 2007*] to resolve the outlines of the melting region. *Wang et al. [2009]* applied such techniques to produce a survey of seismic wave speeds in the mantle beneath the Gulf of California. The Gulf hosts a geometrically complex ridge system that creates oceanic crust between Baja California and mainland Mexico; the overall ridge trend is oblique to the spreading direction. Nonetheless, perpendicularly spreading segments are discernible along the ridge, and a model invoking passive mantle upwelling would predict melting and anomalously slow wave speeds beneath these segments. In contrast, *Wang et al. [2009]* find that the slow mantle seismic anomalies are *not* geographically associated with spreading segments, but are instead located at tens to hundreds of kilometers off axis. The authors interpret their findings as evidence of buoyancy-driven mantle upwelling. The geometric complexity of the ridge, and the close juxtaposition of continental crust make the Gulf a setting that requires three-dimensional flow models to elucidate the convective dynamics.

[6] The MELT experiment [*Forsyth et al., 1998a*] was conducted in a simpler tectonic setting of the southern East Pacific Rise (EPR). It revealed a broad, seismically slow region of mantle and interpreted it as a zone of partial melting, with porosity ~1% [*Toomey et al., 1998*]. Various indicators of asymmetry of melt production across the ridge axis were also discovered by the MELT experiment. *Scheirer et al. [1998]* analyzed shipboard measurements of gravity, seamount distribution, and subsidence rate in the MELT region and found consistent asymmetry among these indicators. *Forsyth et al. [1998b]* used Rayleigh wave tomography to image the shear wave velocity structure of the mantle between 20 and 70 km depth in the same geographic area. Their results exhibited a broad region of anomalously slow velocities, centered to the west of the ridge axis, that they attribute to the presence of partial melt. A similar pattern of asymmetry was observed with teleseismic body wave tomography [*Toomey et al., 1998; Hammond and Toomey, 2003*], shear wave splitting [*Wolfe and Solomon, 1998*], and a magnetotelluric survey [*Evans et al., 1999*]. *Dunn and Forsyth [2003]* used short-period Love waves to probe S wave velocity to a depth of ~50 km for up to ~100 km on each side of the axis and found strong cross-ridge asymmetry in the slow anomaly. Together these studies provide a clear

indication that in the MELT region at present, there is more mantle melting and residual mantle porosity on the west side of the southern EPR.

[7] Two studies, *Conder et al.* [2002] and *Toomey et al.* [2002], have sought to model the observed asymmetry at the MELT region by imposing asymmetric boundary conditions on a passive flow model. Both invoke a combination of anomalously hot mantle beneath the Pacific plate, and a large-scale pressure gradient driving mantle from west to east. The authors justify inclusion of these special circumstances by the proximity of the EPR to hot spots of the Pacific Superswell. To reproduce the observed tomographic asymmetry, however, the models require either very rapid, pressure-driven mantle flow across the ridge ( $\sim 30$  cm/yr), or a very large temperature anomaly ( $> 100$  K) that is confined to the mantle beneath the Pacific plate. In the latter case, the modeled asymmetry is critically dependent on the precise depth extent of the imposed thermal anomaly on the inflow boundary. Though the MELT region could be a special case, one expects a more general explanation for the observed asymmetry that requires only moderate external forcing. Furthermore, lateral temperature and melting rate gradients of the magnitude invoked by *Conder et al.* [2002] and *Toomey et al.* [2002] would yield sharp gradients in mantle density, and hence would likely cause buoyancy-driven flow, a scenario not considered by those studies.

[8] Chemical and thermal buoyancy are known to be significant in the balance of stresses in the deeper mantle; they are the main driving forces for mantle convection and plate tectonics [e.g., *Hager and O'Connell*, 1981; *Faccenna and Becker*, 2010]. The role of buoyancy forces beneath mid-ocean ridges remains controversial, however. *Rabinowicz et al.* [1984] presented an early model of convection beneath ridges that was inspired by observations of flow structures in ophiolites [*Nicolas and Violette*, 1982]. They reasoned that because magma has a lower density than the solid mantle, partially molten mantle is buoyant relative to unmelted mantle. *Rabinowicz et al.* [1984] found that this buoyancy, associated with the residual porosity of the mantle, can drive enhanced upwelling and melting, which can result in a self-reinforcing convective feedback. Subsequent investigations included explicit calculation of coupled mantle flow, melting, and magmatic segregation and explored the dynamics of active upwelling beneath MORs [e.g., *Buck and Su*, 1989; *Scott and Stevenson*, 1989; *Spiegelman*, 1996] and extending lithosphere [*Hernlund et al.*, 2008a, 2008b]. *Tackley and Stevenson* [1993] employed these

concepts to produce a model of self-perpetuating volcanism on terrestrial planets. A selection of these contributions are reviewed in more detail below.

[9] All previous studies of active flow beneath MORs have explicitly assumed symmetry across the ridge axis. However, buoyancy-driven flows are known to produce symmetry-breaking behavior in fluid systems [e.g., *Turner*, 1973]. As an illustration of this, consider the end-member case where buoyancy forces in a partially molten aggregate are much greater than the stresses imposed by plate motion: upwelling will be centered on the regions of maximum buoyancy, rather than aligned with the zone of plate divergence. If buoyancy created by melting is important, we should expect that small, across-axis gradients in mantle temperature, fertility, or dynamic pressure could lead to the development of strong asymmetry in mantle flow. This expectation is borne out by new calculations presented here, and may provide a physical framework in which to better explain tomographic observations.

## 2. Previous Geodynamic Models of Active Flow at MORs

[10] Previous models of active flow beneath mid-ocean ridges can be divided into two categories: single- and two-phase models. In single-phase models, equations derived from conservation principles are used to compute the creeping, incompressible flow of the solid mantle only. In some cases, single-phase models use a parametrization of magmatic transport to compute the rate of crust formation and the residual mantle porosity [e.g., *McKenzie*, 1985]. Two-phase models, in contrast, solve conservation equations for the interpenetrating flows of the creeping mantle and liquid magma. The magma is assumed to flow through the pores spaces between grains of the mantle. Both phases are independently incompressible, but within a volume of mantle containing liquid and solid, the liquid-filled pore network can exhale or inhale (by compacting or dilating) such that there is a negative or positive divergence of solid flow at the continuum scale. Both single- and two-phase models can compute a spatially variable bulk density based on the local porosity, temperature, and composition, however only two-phase models are consistent representations of the dynamic porosity in a natural magma/mantle system.

[11] The first computational study of active convection at MORs, by *Rabinowicz et al.* [1984], used a 2-D, single-phase formulation. They imposed an

aggregate density decrease in the melting region assuming 5% retained porosity; the melting region was defined with one of two recipes. They concluded that for mantle viscosity of  $10^{18}$  Pa s, active upwelling makes a significant but not dominant contribution, whereas at  $10^{17}$  Pa s, active convection dominates and upwelling is focused to a narrow zone. This conclusion is roughly consistent with all subsequent work on the subject. *Sotin and Parmentier* [1989] also used parameterized melt transport, but allowed for spatially variable porosity, and incorporated chemical depletion buoyancy into calculations. *Parmentier and Phipps Morgan* [1990] and *Sparks and Parmentier* [1993] computed a single-phase model in three dimensions, prescribed instantaneous and complete melt extraction, and considered compositional and thermal buoyancy, but not buoyancy from residual porosity. These studies used constant (or piecewise constant) mantle viscosity. Recent single-phase models have used a temperature-, pressure-, composition-, and porosity-dependent, non-Newtonian viscosity to model features such as off-axis volcanic chains [*Ballmer et al.*, 2009].

[12] Two-phase models are more challenging to compute, but are more realistic than single-phase models. They capture magmatic flow and predict the distribution of porosity based on a balance between melting and magmatic segregation. This allows the aggregate density to be computed consistently throughout the domain. *Buck and Su* [1989] introduced temperature- and porosity-dependent mantle viscosity into a 2-D model with Darcian melt segregation. They obtained a sharply localized upwelling beneath the ridge axis, and mantle recirculation at its flanks. Their choice of parameters yielded a porosity of ~25% in the upwelling region. *Scott and Stevenson* [1989] took a similar approach, but applied a piecewise constant mantle viscosity. They explored a larger parameter space than did *Buck and Su* [1989], and presented a reduced analytical model of active flow. *Spiegelman* [1993] assumed constant mantle viscosity in order to decouple the incompressible and irrotational components of the mantle flow field. He obtained solutions for the irrotational component that, in contrast to previous work, incorporate viscous compaction stresses. He derived an inhomogeneous biharmonic equation for the incompressible part, and rescaled it to obtain a dimensionless number analogous to the Rayleigh number, but for buoyancy arising from residual porosity. *Spiegelman* [1993, 1996] presented end-member solutions for large and small values of this number. *Choblet and Parmentier* [2001] constructed a three-dimensional model of

active flow with viscosity and bulk density both dependent on porosity and depletion. That study incorporated Darcian magmatic flow, but neglect compaction and associated stresses. Other authors have considered the two-phase dynamics of diapirs and plumes away from ridges [*Tackley and Stevenson*, 1993; *Ghods and Arkani-Hamed*, 2002; *Schmeling*, 2010].

[13] All previous models of active flow at MORs have assumed symmetry of flow across the ridge axis. The authors performed computations on a domain with one boundary aligned with a vertical line (or plane) directly beneath the ridge axis, where a reflection boundary condition was applied. While their results show that significant active upwelling is expected for mantle viscosities below  $\sim 10^{19}$  Pa s, they do not address the seismic observations of an asymmetrical distribution of mantle flow and porosity that are reviewed above.

[14] Work presented here explores the development of asymmetry in active flow models of coupled magma/mantle dynamics with a domain that straddles the ridge axis. These models account for buoyancy arising from residual porosity *only*, but represent a fully consistent solution of the magmadynamics equations of *McKenzie* [1984]. An earlier version of this model system was presented by *Katz* [2008]; that work incorporated the Enthalpy Method to transparently account for melting/freezing in a two-phase, two-component, energy-conserving system in thermodynamic equilibrium. The models presented here incorporate temperature- and porosity-dependent viscosity. This and other differences from *Katz* [2008] are described in section 3. Section 4 extends the scaling argument of *Spiegelman* [1993] to obtain a dimensionless ratio analogous to the Rayleigh number. Section 5 presents new results on convective vigor and crustal production for comparison with past studies. It then explains the model response to asymmetrical forcing by lateral temperature and compositional gradients, as well as ridge migration. Section 6 discusses present results in the context of observations and previous work, and speculates on how additional model complexity would modify results.

### 3. Model Description

[15] The models presented below are an extension of those described by *Katz* [2008]. They are the result of numerical solution of a set of coupled partial differential equations, representing conservation of mass, momentum, energy, and com-

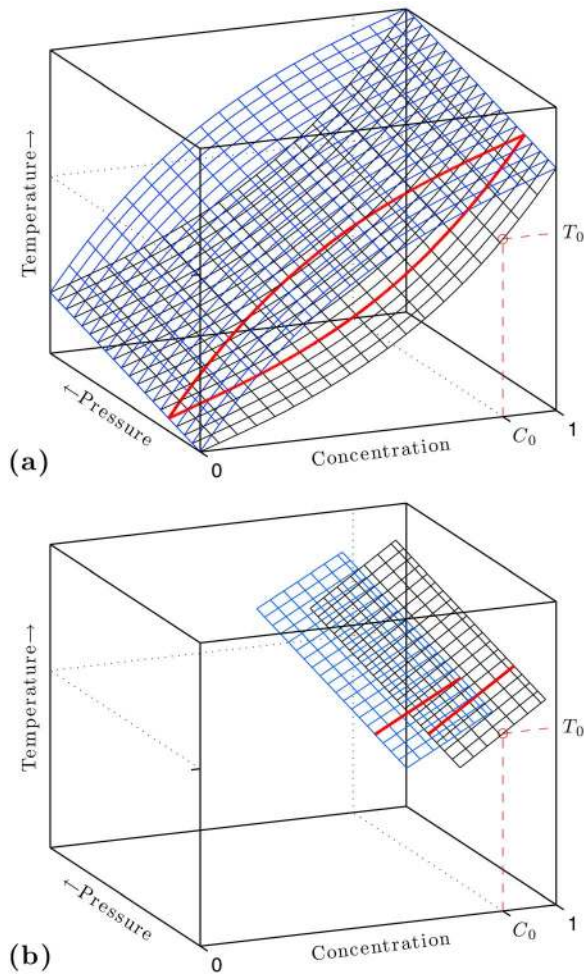


**Figure 1.** Phase diagrams for the two-phase, two-component system. The black mesh represents the solidus temperature as a function of pressure and composition; the blue mesh represents the liquidus temperature. Solid red lines highlight the liquidus and solidus at one particular value of pressure. Along lines of constant composition, the change in the liquidus and solidus surfaces is given by the Clausius–Clapeyron parameter,  $dP/dT|_C = \gamma$ . (a) Solubility loop phase diagram as implemented by Katz [2008]. (b) Liquidus and solidus surfaces linearized about  $C_0$ . The slopes at constant pressure are given by  $M_L$  and  $M_S$  for the liquidus and solidus, respectively.

position in a two-phase, two-component medium. The equations, presented in Appendix A, are a reformulated version of the set derived by McKenzie [1984], and subsequently by other authors with minor differences [e.g., Fowler, 1985; Ribe, 1985b; Scott and Stevenson, 1986; Bercovici et al., 2001]. Use of the Enthalpy Method [e.g., Alexiades and Solomon, 1993] as a means for computing the evolution of thermochemical variables in magma-

dynamic simulations was introduced by Katz [2008] and is continued here. Numerical solutions are obtained using the Portable Extensible Toolkit for Scientific Computation; the discretization, solution strategy, and algorithms are outlined in section A5.

[16] There are several important differences between the current models and past work. In this manuscript I examine the effects of buoyancy forces on the flow of the matrix phase, whereas Katz [2008] considered only passively driven mantle flow. Mathematical details of the buoyancy terms in the governing equations can be found in Appendix A. To model active mantle convection in a physically reasonable way (i.e., respecting the rigidity of the lithosphere), I incorporate a temperature-dependent shear viscosity, representing deformation by diffusion creep [e.g., Karato and Wu, 1993]. The shear viscosity in the present models also depends on porosity [e.g., Hirth and Kohlstedt, 2003]. Models described by Katz [2008] used constant shear viscosity. Constitutive relations employed in the present models are detailed below. This is preceded by an explanation of the highly simplified petrological relations parameterized as a two-component phase diagram, and followed by a discussion of the means of melt extraction to the model crust.

[17] Two-phase mid-ocean ridge models by Katz [2008] as well those by previous workers [Buck and Su, 1989; Scott and Stevenson, 1989; Spiegelman, 1996; Ghods and Arkani-Hamed, 2000] have assumed mirror symmetry across the vertical boundary beneath the ridge axis. Motivated by an interest in observed asymmetries in tomographic images [e.g., Forsyth et al., 1998b; Dunn and Forsyth, 2003], I have extended the simulation code described by Katz [2008] to optionally model both sides of the ridge axis, without any assumption regarding symmetry. Indeed, this allows for symmetry-breaking boundary conditions such as ridge migration and large-scale temperature gradients; these are explored in detail below.

### 3.1. Petrology

[18] The petrological model is based on that employed by Katz [2008]: temperature-pressure-composition relations in an equilibrium, two-component system are parameterized with a phase diagram. The solidus and liquidus temperatures increase linearly with pressure according to the Clapeyron slope. In the work by Katz [2008], the phase compositions were described with cubic polynomials of temperature; in the current models these relations

are linearized about the ambient mantle concentration  $C_0$ , as shown in Figure 1b. The surfaces are defined by

$$C_S = C_0 + \frac{T - (T_0 + P_f/\gamma)}{M_S}, \quad (1a)$$

$$C_L = C_0 - \Delta C + \frac{T - (T_0 + P_f/\gamma)}{M_L}. \quad (1b)$$

$C_S$  and  $C_L$  define the compositions of the solid and liquid, respectively, where they coexist in thermodynamic equilibrium;  $T_0$  is the reference solidus temperature at zero pressure and ambient mantle composition  $C_0$ ;  $\Delta C$  is the reference composition difference between solidus and liquidus surfaces at temperature  $T_0$ ;  $P_f$  is the pressure of the fluid; and  $\gamma = dP/dT|_C$  is the Clapeyron slope (assumed equal for both phases). The change in temperature with composition at fixed pressure is given by  $M_S$  and  $M_L$  for the solidus and the liquidus, respectively.

[19] Katz [2008] chose  $C_0$ , the concentration of the *less fusible* phase in the ambient mantle, to be 12 percent by mass. In the current model I choose  $C_0$  to be 85 percent; I then set the solidus temperature  $T_0$  for composition  $C_0$  and mantle potential temperature  $T_m$  so as to impose the bottom of the melting regime at a depth of ~60 km. The different values of  $C_0$  make no difference to the dynamics of the system, though the current choice is consistent with an asthenosphere that is composed mainly of olivine, which is less fusible than other mantle minerals.

[20] It would be a mistake, however, to quantitatively map the compositional space of the current models to actual phase relations under mantle melting. The purpose of this simple petrological system is to provide a basis for identifying “enriched” ( $C$  smaller) and “depleted” ( $C$  larger) compositions, and to hence enable the model to capture a minimal aspect of chemical variability. Furthermore, the assumption of thermodynamic equilibrium made here is problematic in terms of fidelity to the natural mantle system. This assumption is justified by the aim of the current work to study the coupled fluid dynamics of the magma/mantle system, which requires a petrologically reasonable, energy conservative, internally consistent, and simple approach to mantle melting/freezing.

[21] The solidus equation (1a) can be combined with the linearized expression for the adiabatic temperature gradient,  $T(z) \approx T_m (1 + \alpha \rho z / c_P)$ , to give the initial depth of melting. For a homogeneous mantle

of composition  $C_0$  and potential temperature  $T_m$ , the result is

$$z_m = \frac{\gamma c_P (T_m - T_0)}{g(\rho c_P - \gamma T_m \alpha)}, \quad (2)$$

where  $\rho$  is the mean density of a the mantle column,  $\alpha$  is the coefficient of thermal expansivity, and  $c_P$  is the specific heat capacity. Using  $\gamma = 60^{-1}$  GPa/K,  $T_m = 1648$  K,  $T_0 = 1565$  K,  $\rho = 3000$  kg/m<sup>3</sup>,  $g = 10$  m/s<sup>2</sup>,  $\alpha = 3 \times 10^{-5}$  K<sup>-1</sup>, and  $c_P = 1200$  J/kg/K, I obtain  $z_m = 60$  km.

### 3.2. Rheology

[22] Experimental studies of mantle rheology indicate that it varies with parameters including temperature, pressure, strain rate, melt fraction, and water content [e.g., Hirth and Kohlstedt, 2003]. These dependencies themselves vary as a function of the mode of deformation. New evidence from analogue experiments [Takei, 2010] and homogenization theory [Takei and Holtzman, 2009a, 2009b, 2009c] suggest that the mantle is viscously anisotropic. While these complexities could have significant consequences for coupled magma/mantle dynamics, to keep models relatively simple here, I capture the only the leading-order variation in mantle viscosity, which is isotropic.

#### 3.2.1. Shear Viscosity

[23] The shear viscosity is taken to vary with temperature and porosity according to

$$\eta = \eta_0 \exp \left[ \frac{E^*}{R} \left( \frac{1}{T} - \frac{1}{T_{\eta_0}} \right) - \lambda \phi \right], \quad (3)$$

where  $E^*$  is the activation energy,  $R$  is the universal gas constant,  $T$  is the temperature in Kelvin,  $\lambda$  is a positive constant, and  $\phi$  is the porosity.  $T_{\eta_0}$  is a constant, set equal to the temperature at which the mantle first crosses the solidus,  $T_{\eta_0} = T_m \exp(\alpha g z_m / c_P)$ , with  $z_m$  from equation (2). Hence  $\eta_0$  is the viscosity just below the melting region. For numerical efficiency, variation of viscosity in the present models is limited by an upper bound of  $10^{25}$  Pa s; this limit is sufficiently high to have a negligible effect on the mantle flow field. No lower bound is imposed.

[24] Equation (3) can be thought of as a simplified parametrization of diffusion creep viscosity. The temperature dependence allows for the important

effect of rigid lithospheric plates. By incorporating a porosity dependence, the emergence of localized porosity structures, as observed in experiments and theory [Kohlstedt and Holtzman, 2009], are not excluded a priori. As we shall see in section 6.3, however, under the current rheological formulation, a mechanical porosity-banding instability is not predicted by models.

### 3.2.2. Bulk Viscosity

[25] The bulk viscosity is taken to vary with temperature and porosity according to

$$\zeta = \zeta_0 \exp \left[ \frac{E^*}{R} \left( \frac{1}{T} - \frac{1}{T_{\eta_0}} \right) \right] \phi^{-1}, \quad (4)$$

where  $\zeta_0$  is a reference value of bulk viscosity. The Arrhenius factor controls the shear viscosity of the solid grains, and hence appears in the relation for bulk viscosity as well. The form of (4) is consistent with theoretical predictions [e.g., Batchelor, 1967; Schmeling, 2000; Bercovici et al., 2001; Hewitt and Fowler, 2008; Simpson et al., 2010a] and experimental constraints [Cooper, 1990] on the variation of bulk viscosity. These studies indicate that  $\zeta_0$  should be equal to  $\eta_0$  times an order 1 constant.

[26] Katz [2008] neglected the temperature dependence of viscosity and showed how the magnitude of the bulk viscosity is a control on sublithospheric melt focusing to the ridge axis [Sparks and Parmentier, 1991]; this is confirmed by current models with the rheology as given above. In the calculations presented below, unless otherwise indicated, I have taken  $\zeta_0 = 10^{19}$  Pa s. This choice may be inconsistent with theoretical predictions [e.g., Simpson et al., 2010b], however it yields compaction lengths within the partially molten region that can be resolved numerically, and it ensures a high focusing efficiency by minimizing thermomagmatic erosion into the base of the lithosphere [see Katz, 2008, Figure 4]. Efficient focusing promotes the attainment of a steady state in numerical solutions; hence it facilitates investigation of the convective dynamics of the subridge mantle.

### 3.3. Melt Extraction at the Ridge

[27] The present models also differ from those of Katz [2008] in the way that melt is extracted at the ridge axis. In past work, magma escaped through

the upper boundary of the domain via a narrow, imposed “window” at the ridge axis. This approach, though simple, has various problems; in particular, it precludes the use of slower spreading rates and variable viscosity. In the present models, magma is extracted through a “dike.” In the computational domain, this is implemented as a boundary condition between grid cells, directly beneath the ridge axis. This internal boundary begins between the shallowest cells with nonzero porosity, and extends a fixed number of cells downward. The choice to impose the extent of the dike in terms of a number of grid cells rather than a physical length is based on technical rather than physical grounds. Three or four grid cells, independent of the grid spacing, are the minimum number required such that entry into the dike is not a rate-limiting factor for melt extraction.

[28] The grid cells that are adjacent to the dike experience a fluid pressure gradient that is proportional to the difference between the lithostatic pressure outside the dike and the magma-static pressure within it

$$\left. \frac{dP_f}{dx} \right|_{\text{dike}} = \pm \mathcal{F} \frac{\Delta \rho g z}{\Delta x/2}, \quad (5)$$

where  $\mathcal{F}$  is a fraction between zero and unity,  $\Delta x/2$  is the  $x$  distance between the center of a grid cell and its edge. The case of  $\mathcal{F} = 1$  applies if the dike is continuously open all the way to the surface; assuming dynamic forces are negligible, this case provides an upper bound on the pressure gradient. Reducing  $\mathcal{F}$  leads to larger porosity and smaller magmatic flow speed in the immediate neighborhood of the dike. I use  $\mathcal{F} = 0.005$  to obtain solutions reported below; this value is large enough to maintain low porosity beneath the ridge axis, but small enough to avoid a suction effect being felt beyond the immediate neighborhood of the dike.

[29] Magma that enters the dike (by crossing the internal boundary between cells) is immediately extracted from the domain and pooled, along with the composition and enthalpy that it carries. The rate of extraction and the composition of the extracted melt is recorded at each time step.

## 4. Scaling Analysis

[30] If gradients of buoyancy in the mantle beneath a mid-ocean ridges are of the same order as gradients in the viscous stresses arising from plate-induced mantle flow, then there will be a component of active mantle convection beneath the ridge axis

[Rabinowicz *et al.*, 1987]. Buoyancy-driven convection is typically studied in terms of the dimensionless Rayleigh number, which is the ratio of factors driving convection to those resisting it [e.g., Turner, 1973]. A parameter similar to the Rayleigh number was derived by Spiegelman [1993] for the mantle beneath a mid-ocean ridge, where buoyancy forces arise from the presence of melt. Here I extend that analysis in order to obtain the scaling of active upwelling velocity with problem parameters.

[31] In the absence of melt, shearing flow of the crystalline mantle on tectonic length and time scales is governed by the Stokes equation. Appendix A reviews the derivation of the corresponding equation for the case of a *two-phase* system, with small amounts of melt present in the pore spaces between mantle grains. In terms of dimensional variables, this equation becomes

$$\nabla P = \nabla \cdot \eta (\nabla \mathbf{v}_m + \nabla \mathbf{v}_m^T) - \phi \Delta \rho \mathbf{g}, \quad (6)$$

where  $P$  is a dynamic pressure,  $\eta$  is the shear viscosity of the two-phase aggregate,  $\mathbf{v}_m$  is the mantle velocity,  $\Delta \rho$  is the difference in density between the mantle and the magma, and  $\mathbf{g}$  is the gravity vector. This equation states that pressure gradients are balanced by viscous stresses and a body force arising from buoyancy. Assuming the phase densities are constant in space and time, the buoyancy force on the two-phase aggregate is due solely to the porosity.

[32] To simplify, I further assume that beneath the lithosphere, where mantle temperatures are approximately adiabatic, the mantle viscosity is constant. This approximation, applied *in this section only*, neglects the effects temperature and porosity, which are included in simulations, as well as lithostatic pressure and water content [e.g., Hirth and Kohlstedt, 2003]. While the former may be a good assumption in the shallow asthenosphere, the latter two are questionable; even small amounts of water in crystals has a large effect on their viscosity. Choblet and Parmentier [2001] found that the rheological effects of water on convection beneath ridges are significant. Neglecting viscosity variation due to porosity is less troublesome; simulations show that it does not lead to large variations within the melting region. There are other limitations associated with these approximations, and I do not expect this scaling analysis to be strictly accurate for the mantle. It will provide a basis, however, for understanding current simulations (that employ temperature- and porosity-dependent viscosity *throughout* the domain) and may give some insight into the physical regime relevant for the Earth.

[33] For constant  $\eta = \eta_0$ , I take the curl of equation (6) to obtain, within the adiabatic asthenosphere,

$$\eta_0 \nabla^2 \omega = \Delta \rho g \partial_x \phi, \quad (7)$$

where  $\omega = \nabla \times \mathbf{v}_m$  and  $\partial_x$  indicates a partial derivative in the  $x$  direction. This is the vorticity equation and states that lateral gradients in buoyancy are an internal source of vorticity. Vorticity is also generated by the boundary conditions, the spreading tectonic plates. To estimate the importance of buoyancy versus spreading-induced vorticity, following Spiegelman [1993] I rescale variables with characteristic scales:

$$\tilde{x} = h_0, \quad \tilde{\phi} = \phi_0, \quad \tilde{\omega} = \frac{U_0}{h_0}. \quad (8)$$

The characteristic scale for distance is  $h_0$ , the height of the melting column. The characteristic scale for porosity is  $\phi_0$ , which is a representative value for the column of rock beneath the ridge axis. The characteristic scale for vorticity is  $U_0/h_0$ , with  $U_0$  the half-spreading rate. Applying these scales and dropping primes from dimensionless variables gives

$$\nabla^2 \omega = \mathcal{V} \partial_x \phi, \quad \text{with} \quad \mathcal{V} = \frac{\Delta \rho g \phi_0 h_0^2}{\eta_0 U_0}, \quad (9)$$

where  $\mathcal{V}$  is a dimensionless number analogous to the Rayleigh number in thermal convection. This result was obtained by Spiegelman [1993]; I extend it by constraining the characteristic porosity  $\phi_0$  using a result from Ribe [1985a]. That work considered an upwelling, melting column of mantle rock and neglected compaction stresses to obtain

$$\phi(z) = \left[ \frac{\mu W_0 F}{K_0 \Delta \rho g} \right]^{1/n}, \quad (10)$$

where  $\mu$  is the viscosity of the magma,  $F(z)$  is the degree of melting,  $W_0$  represents the rate of mantle upwelling at the base of the column, and  $K_0$  and  $n$  are associated with the permeability-porosity relation,  $K = K_0 \phi^n$ . Since the contribution of buoyancy to upwelling is a priori unknown, I will take the upwelling rate  $W_0$  equal to  $U_0$  for convenience, and remain cognizant that this will be an underestimate (though the exponent  $1/n$  reduces the impact of this error). Furthermore, since I seek an estimate of the characteristic porosity, I will take a representative value for degree of melting,  $F_0$ , equal to the degree of melting at the top of the column.

[34] Incorporating these modifications, taking  $n = 3$ , and substituting equation (10) into equation (9) gives

$$\mathcal{V} = \left[ \frac{\Delta \rho g}{U_0} \right]^{2/3} \left[ \frac{\mu F_0}{K_0} \right]^{1/3} \frac{h_0^2}{\eta_0}. \quad (11)$$



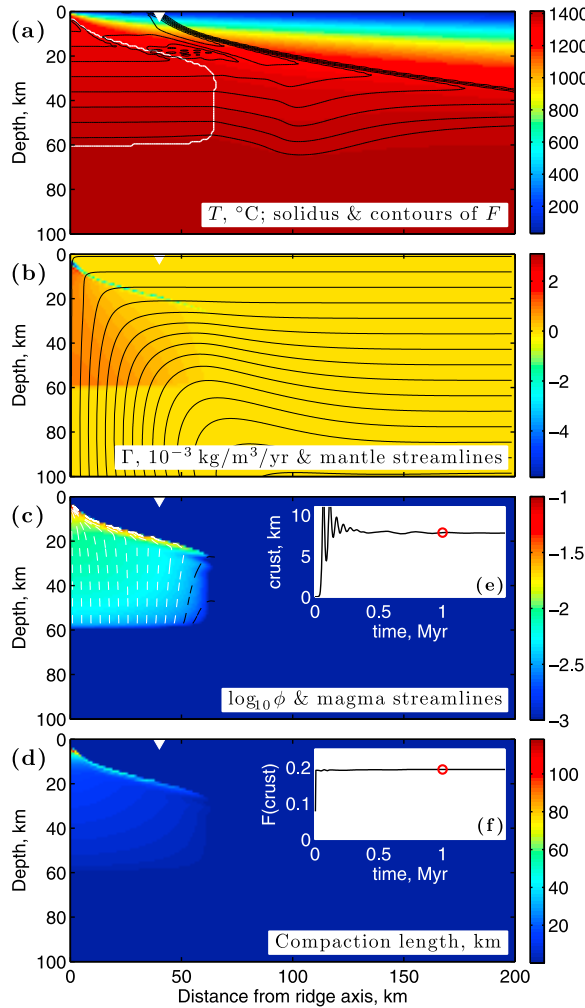


**Figure 2.** Results of a simulation with half-spreading rate  $U_0 = 4$  cm/yr, reference viscosities  $\eta_0 = 10^{18}$  Pa s and  $\zeta_0 = 10^{19}$  Pa s, permeability constant  $K_0 = 10^{-7}$  m<sup>2</sup>, potential temperature of 1375°C, and other parameters as given in Table B2. (a–d) Various fields obtained from the calculation after 1 Ma of simulated time. White triangles show the distance of plate motion over this period. Black curves in Figure 2a connect points of constant degree of melting  $F = (C_m - C_0)/(C_m - C_f)$ , starting with 1% at the bottom of the melting region and increasing in steps of 2.5%; these lines cluster along the edge of the region that has experienced melting since  $t = 0$ . In this model,  $F_{\max} = 20\%$ . (e) Crustal thickness as a function of time. The red point marks the crustal thickness at 1 Ma. (f) The apparent degree of melting corresponding to the composition of the crust is approximately constant throughout the simulation. This was computed using  $F_{\text{crust}} = (C_{\text{crust}} + \Delta C - C_0)/\Delta C$ .

The dimensionless number  $\mathcal{V}$  predicts how the relative importance of active upwelling scales with problem parameters. It is more informative than the version presented by *Spiegelman* [1993] because it expands the dependence of  $\phi_0$  to parameters

that can be estimated from observations or experiments. When  $\mathcal{V} \ll 1$ , equation (11) predicts a passive mantle flow regime, whereas when  $\mathcal{V} \gg 1$ , buoyancy-driven flow will dominate. As we shall see in the results section 5.1, the vigor parameter can provide a quantitative prediction of upwelling rate relative to the spreading rate.

[35] Inspection of equation (11) shows that the melting column height and mantle viscosity are the primary controls on the vigor parameter. The spreading rate appears explicitly as  $U_0^{-2/3}$ , indicating a decrease in the relative importance of active convection for faster spreading. However, for slow and ultraslow spreading centers, the column height  $h_0$  decreases sharply with decreasing spreading rate, building in an implicit dependence on  $U_0$ .

## 5. Results

[36] Figure 2 shows output at  $t = 1$  Ma from a representative simulation with buoyancy-driven mantle flow. The calculation was initialized following the steps made by *Katz* [2008] and *Ghods and Arkani-Hamed* [2000]: (1) the steady state mantle flow, temperature, and porosity are calculated assuming passive upwelling and zero permeability; (2) the enthalpy field is reduced by the latent heat at each point [ $\mathcal{H} \leftarrow (\mathcal{H} - \rho L \phi)$ ]; (3) the bulk composition is set equal to the mantle composition [ $C \leftarrow C_m$ ]; and (4) the porosity is set to zero everywhere [ $\phi \leftarrow 0$ ]. At later times, the history of this initial condition is reflected in the sharp gradient in the degree of melting  $F$ , contoured in Figure 2a; this feature marks what was the edge of the melting region at  $t = 0$ .

[37] A solution to the governing equations comprises mantle and magmatic flow fields, dynamic and compaction pressure, temperature, porosity, and the bulk, magma, and mantle compositions; some of these outputs are shown in Figure 2 (see caption for details). Melting rate can be obtained from solutions at two consecutive time steps as  $\Gamma = \partial \phi / \partial t - \nabla \cdot (1 - \phi) \mathbf{v}_m$  and is shown in Figure 2b.

[38] Streamlines in Figure 2b show that for a background shear viscosity of  $\eta_0 = 10^{18}$  Pa s and residual mantle porosity of  $\sim 1\%$ , mantle flow is not drastically different from the typical pattern of passive upwelling. The melting region appears roughly triangular, however its width is diminished relative to the case of passive upwelling only. The choice of  $\zeta_0 = 10^{19}$  Pa s ensures that the focusing efficiency is high [*Katz*, 2008]; it is also responsible for the large values of compaction

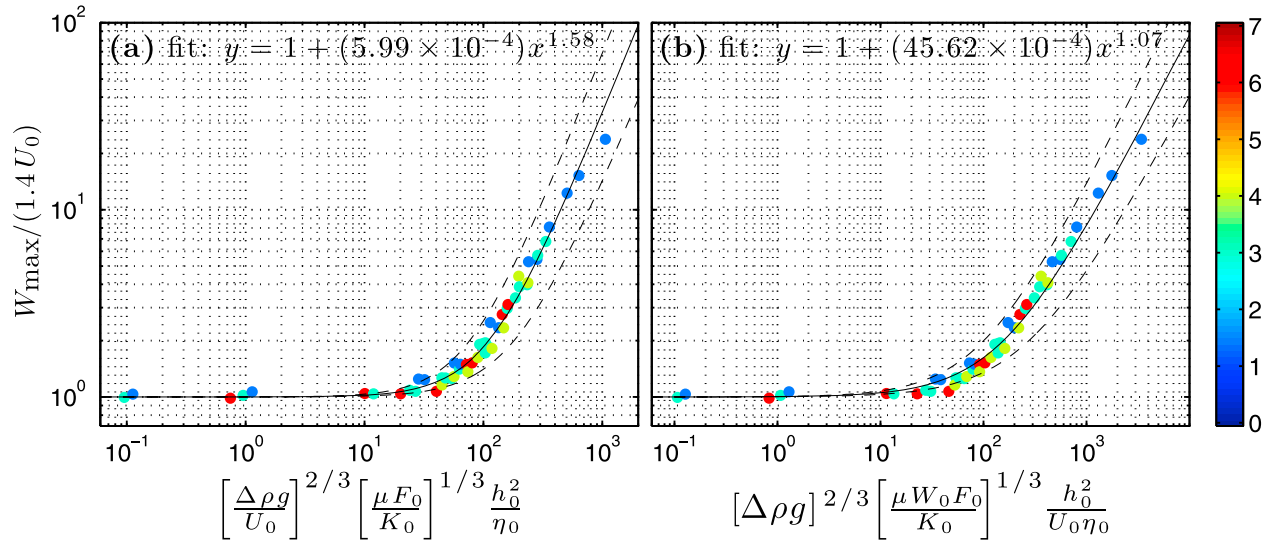


**Figure 3.** Calculated maximum upwelling rate from simulations, normalized by the upwelling rate expected for passive flow ( $1.4U_0$ ) and plotted against two versions of the vigor parameter. Point color represents half-spreading rate in cm/yr, according to the color bar at right. (a) The  $x$  axis is  $\mathcal{V}$  as defined in equation (11). (b) The  $x$  axis is  $\mathcal{V}_W$  in which the background porosity  $\phi_0$  is calculated using the maximum upwelling rate obtained from the simulation. Solid lines in Figures 3a and 3b are lines of best fit, calculated using nonlinear least squares error minimization to the function  $y = 1 - ax^b$ . Dashed lines represent the 95% confidence interval on the fit. The formula for the solid lines is given in the plot; dashed curves are given by  $y = 1 - (3.82 \times 10^{-4})x^{1.52}$  and  $y = 1 - (8.07 \times 10^{-4})x^{1.64}$  in Figure 3a and  $y = 1 - (3.18 \times 10^{-3})x^{1.02}$  and  $y = 1 - (5.95 \times 10^{-3})x^{1.11}$  in Figure 3b. The simulations use a half-ridge domain of 200 km width by 100 km height, with a grid resolution of 1 km in each direction.

length shown in Figure 2d. The compaction length is given by

$$\delta_c = \sqrt{\frac{K(\zeta + 4\eta/3)}{\mu}} \approx \left\{ \frac{\zeta_0 K_0 \phi^{n-1}}{\mu} \exp \left[ \frac{E^*}{R} \left( \frac{1}{T} - \frac{1}{T_0} \right) \right] \right\}^{1/2} \quad (12)$$

when  $\phi \ll 1$  and  $\zeta_0 \gtrsim 4\eta_0/3$ . For the parameters used in the calculation shown in Figure 2,  $\phi \sim 0.01$  and  $T \sim T_0$ , the compaction length is on the order of 10 km.

[39] In sections 5.1–5.3, I describe results from suites of models, where each model is a variation of the one in Figure 2. Section 5.1 quantifies the relationship between the vigor parameter  $\mathcal{V}$  and simulation results on the rate of mantle upwelling. Section 5.2 considers variation in crustal production with problem parameters. Section 5.3 considers the symmetry breaking by active convection beneath a mid-ocean ridge. In section 6, these results are interpreted in terms of geophysical predictions and consistency with observations.

### 5.1. Convective Vigor

[40] The contribution of active convection to upwelling beneath the ridge should be related to the

importance of the buoyancy term in equation (6), hence it should be possible to predict the rate of upwelling using the vigor parameter  $\mathcal{V}$ . This parameter was introduced in a simpler form by *Spiegelman* [1993], but he presented mantle flow for only two end-member cases,  $\mathcal{V} \ll 1$  and  $\mathcal{V} \gg 1$ . A natural system may exist anywhere along this spectrum; I test for a quantitative relationship between  $\mathcal{V}$  and upwelling rate using a suite of numerical models.

[41] Calculations of passive, variable viscosity mantle flow produce a relationship between half-spreading rate and maximum mantle upwelling rate given by  $W_{\max} \approx 1.4U_0$ . I therefore seek to quantify the contribution of active upwelling by considering the ratio  $W_{\max}/(1.4U_0)$  for different values of  $\mathcal{V}$ . This data from a suite of simulations is shown in Figure 3. Figure 3a demonstrates that there is a clear relationship between the vigor parameter and the contribution of buoyancy to upwelling. The colored points represent model results for half-spreading rates of 1.5, 3, 4, and 6 cm/yr, with viscosity parameter  $\eta_0$  ranging from  $2 \times 10^{17}$  to  $10^{21}$  Pa s, permeability parameter  $K_0$  ranging from  $10^{-8}$  to  $10^{-6}$  m<sup>2</sup>, and other parameter variations as given in Table B1. The  $y$  values are spread over more than an order of magnitude; by plotting against  $\mathcal{V}$ , they collapse onto a line. Figure 3b shows that the data

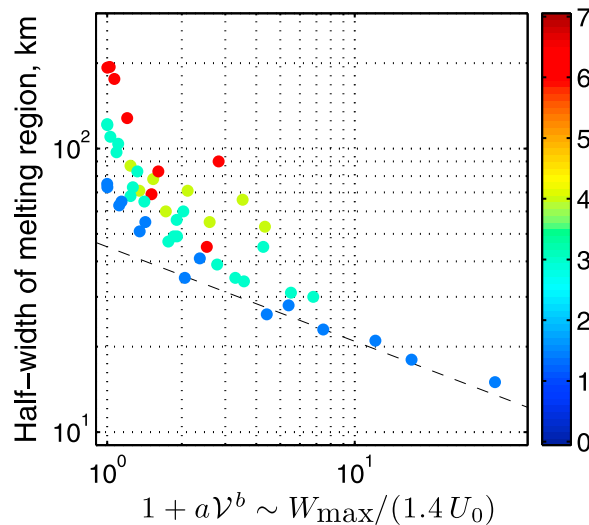


**Figure 4.** Melting region half-width as a function of  $1 + a\mathcal{V}^b$  with  $\mathcal{V}$  as defined in equation (11) and with  $a, b$  from the best fitting line in Figure 3a for different values of half-spreading rate  $U_0$ . As in Figure 3, colors correspond to half-spreading rate in cm/yr. The dashed line is a plot of  $y = 50x^{-1/3}$ .

collapse is equally tight if plotted against the dimensionless number  $\mathcal{V}_W = \mathcal{V}(W_0/U_0)^{1/n}$ . This is a modified vigor parameter that includes the mantle upwelling velocity extracted from each simulation result (i.e., it does not assume that  $W_0 \approx U_0$ ).

[42] The solid lines in Figure 3 are best fit regressions of the form  $W_{\max}/(1.4U_0) = 1 + a\mathcal{V}^b$ , where  $a$  and  $b$  are fit parameters. Values for these parameters were obtained by nonlinear least squares error minimization (see caption of Figure 3). Assuming that the components of  $\mathcal{V}$  are independently constrained by observations, experiments, and thermodynamic calculations, then the lines of best fit in Figure 3 can be used to predict the contribution to mantle upwelling of the buoyancy from residual mantle porosity (explicitly for the fit from Figure 3a, implicitly for that of Figure 3b). More generally, however, these “empirical” relationships provide a means for assessing the dynamical consequences of hypotheses on mantle properties and processes. It is interesting to note that the relationship between  $W_{\max}/(1.4U_0)$  and  $\mathcal{V}_W$  is nearly linear in the regime where active upwelling is important (Figure 3b); this suggests that the assumptions made in deriving the scaling parameter are appropriate in the context of current simulations.

[43] The data collapse obtained by plotting against  $1 + a\mathcal{V}^b$  suggests that the parameter space of possible active upwelling scenarios is smaller than

anticipated: instead of having dimensions of the number of ill-constrained model parameters, Figure 3 suggests that it is a one-dimensional space described by  $\mathcal{V}$  (or  $\mathcal{V}_W$ ). Within the context of the physics that is captured by these models, this dimensionless number quantifies how parameter values can trade off. For example, the effect of doubling the mantle viscosity parameter  $\eta_0$  is equivalent to the effect of a factor  $2^n$  change in permeability parameter  $K_0$ , where  $n$  is the exponent in the permeability-porosity relation. I use this and other trade-offs quantified by  $\mathcal{V}$  to explore the behavioral space of the simulations without varying all of the parameters; in sections 5.2 and 5.3, only the parameter  $\eta_0$  is varied between simulations, but the results can be approximately mapped to variations in the vigor of active convection.

[44] Figure 4 shows the half-width of the melting regime from the same set of simulations that was used to construct Figure 3. The data are plotted against  $1 - a\mathcal{V}^b$ , which approximates the ratio of the maximum upwelling rate to that expected for passive flow. For  $x \rightarrow 1$  (passive limit), the data trend toward different  $y$  values, as expected based on spreading rate control of lithospheric thermal structure. With increasing convective vigor this spread decreases, indicating that the width of the melting regime is here controlled by the horizontal length scale of active convection.

## 5.2. Crustal Generation

[45] How does vigor of active convection affect the thickness of crust produced at the ridge axis? If we assume thermodynamic reversibility and neglect the details of melt segregation, the melt productivity  $dF/dz|_S$  of adiabatically upwelling lherzolite is independent of upwelling rate [e.g., *Asimow et al.*, 1997]; one therefore expects that the maximum degree of melting at the top of a melting column,  $\int_{z_m}^{z_1} dF/dz|_S dz$ , does not depend on upwelling rate. A faster upwelling rate should produce a proportionally larger melt production rate  $\Gamma$  beneath the ridge axis. Passive mantle flow, driven by divergence of tectonic plates at the ridge axis, produces a rate of upwelling that scales with the spreading rate. As described in section 5.1, buoyancy forces arising from residual porosity can lead to upwelling at greater rates; if these are substantial relative to the rate of passive flow, buoyancy-driven flow will lead to enhanced melting, and thicker crust.

[46] Figure 5 shows the results of a suite of models with different relative contributions of buoyancy-driven upwelling. Each line corresponds to a single

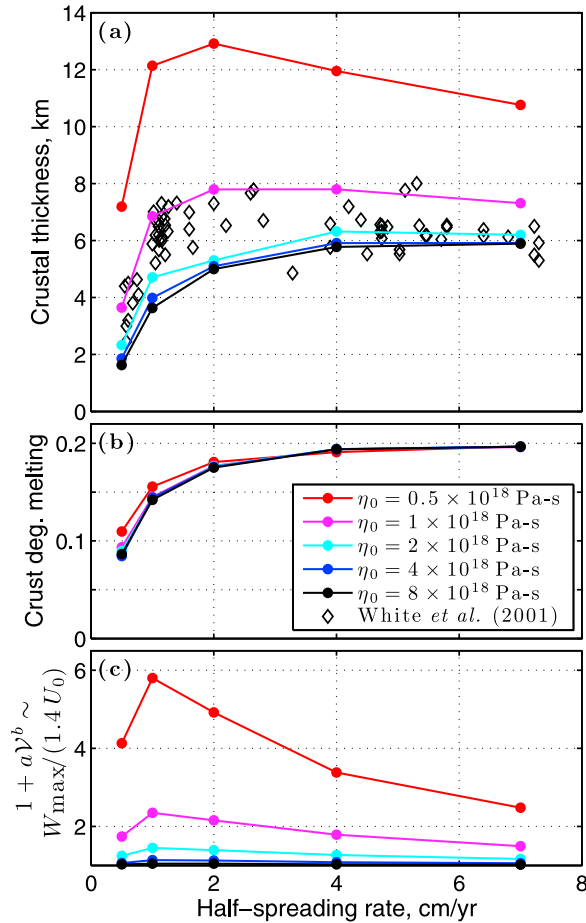


**Figure 5.** Predicted crustal properties from models compared with seismic observations from *White et al.* [2001], plotted against half-spreading rate. Colors represent different values of  $\eta_0$ , as given in the legend. Each point is the average of predicted crustal thickness from  $t = 1.0$  to  $t = 1.5$  Ma of the simulated time. Each model uses  $\zeta_0 = 10^{19}$  Pa s. (a) Crustal thickness. (b) The degree of melting associated with the composition of the crust, calculated as  $F_{\text{crust}} = (C_{\text{crust}} + \Delta C - C_0)/\Delta C$ . (c) The ratio of total upwelling rate to passive upwelling rate, plotted as a function of spreading rate.

value of  $\eta_0$ , and each point on the line corresponds to a different spreading rate. Figure 5a shows crustal thickness as a function of half-spreading rate; the data points are reproduced from *White et al.* [2001], and represent seismic measurements of crustal thickness from spreading ridges around the globe. The black curve in Figure 5a represents models with background viscosity  $\eta_0 = 8 \times 10^{18}$  Pa s; in these calculations, the pattern of upwelling is almost indistinguishable from passive flow. With decreasing  $\eta_0$  (increasing  $\mathcal{V}$ ), subridge mantle upwelling rates increase, and hence crustal thickness increases at any value of half-spreading rate. This effect is pronounced for  $\eta_0$  less than  $2 \times 10^{18}$  Pa s.

[47] Figure 5b shows the mean degree of melting that produces the crust, based on the composition of the crust. This is calculated using  $F_{\text{crust}} = (C_{\text{crust}} + \Delta C - C_0)/\Delta C$ , where  $C_{\text{crust}}(t)$  is the composition of aggregated melts entering the dike at time  $t$  and  $\Delta C$  is the reference compositional difference between the liquidus and solidus. This plot shows that the mean degree of melting is nearly independent of  $\eta_0$ , and hence nearly independent of the component of active upwelling. This is unsurprising, given that  $F$  is controlled by the column height of upwelling mantle at temperatures above the solidus [*Langmuir et al.*, 1992]. At slow spreading rates, the current simulations indicate that active upwelling can modify the vertical balance of advection and diffusion of heat below the ridge axis. This causes a thinning of the thermal boundary layer, an increase in height of the melting column, and an increase in the maximum and the mean degree of melting. At  $U_0 = 0.5$  cm/yr, the maximum difference in melting column height between two simulations from Figure 5 is  $35 - 29 = 6$  km. The simulations produce a mantle-upwelling melt productivity  $dF/dz$  that is nearly constant at 0.35 %/km; multiplying this by 6 km gives a difference in degree of melting of about 2 percent. Note, however, that *Ito and Mahoney* [2005] used a petrological model with variable adiabatic productivity and found that the mean degree of melting varies with the spatial distribution of melting rate, even for a fixed melting column.

[48] A comparison between the data points and model curves in Figure 5a would seem to indicate that a nonnegligible contribution from active upwelling is required to fit the data. It is important to note, however, that the amplitude of these curves is sensitive to a range of ill-constrained model parameters. For example, an increase in mantle potential temperature would lead to thicker crust for the same spreading rate and mantle viscosity structure. A change of parameters in the two-component petrological model used here could have the same effect. Hence in the context of the present model, crustal thickness alone does not permit us to distinguish between a range of active upwelling scenarios. This topic is examined in more detail in section 6.

[49] The variation of crustal thickness with spreading rate at intermediate to fast rates may be useful for making this distinction. The array of data in Figure 5a seems to trend toward smaller values of crustal thickness with increasing spreading rate, above 2 cm/yr. A similar trend is seen in the red and pink curves, representing lower values of viscosity. Figure 5c indicates that in the models, this trend

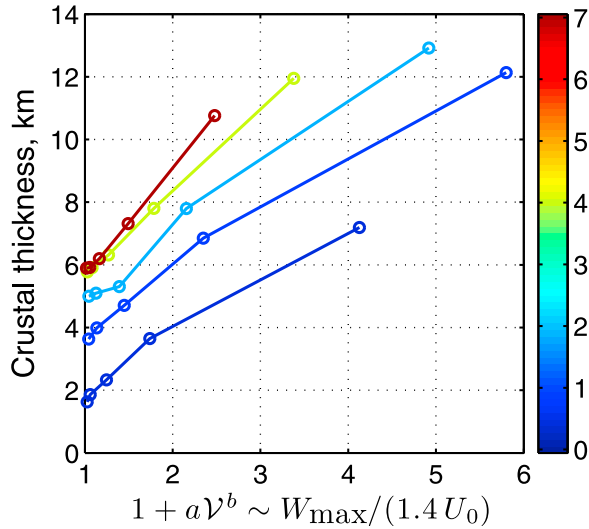


**Figure 6.** Crustal thickness versus  $1 + a\mathcal{V}^b$  for model results shown in Figure 5.  $\mathcal{V}$  is defined in equation (11), and  $a$ ,  $b$  are constants from the best fitting line shown in Figure 3a. Colors indicate half-spreading rate in cm/yr according to the color bar at right.

arises from the decreasing contribution of active upwelling relative to passive upwelling. This can be understood by considering that  $F_{\max}$  is relatively constant over this range of increasing spreading rates, and hence  $\mathcal{V}$  is decreasing. If the decreasing trend in the data is robust, it may provide evidence for a contribution of active upwelling.

[50] Figure 6 shows that at a fixed spreading rate, crustal thickness increases linearly with the contribution of active upwelling. The slope of the lines in Figure 6 are smaller than might be expected, however. At  $W_{\max}/(1.4U_0) = 2$ , the maximum upwelling rate is double its expected value for passive upwelling, and hence one might expect the crustal thickness to have increased by a factor of 2. This doubling does not occur because the distribution of upwelling and melting changes with increasing contribution of buoyancy: the melting region narrows (Figure 4) and upwelling is localized around the zone of maximum buoyancy. As shown in section 5.3, this zone is not necessarily located directly beneath the ridge axis.

### 5.3. Symmetry Breaking by Convection

[51] Plate spreading is clearly an essential aspect of the localization of magma genesis to the region beneath and around mid-ocean ridges. It provides a baseline mantle-upwelling flow that leads to melt production and residual porosity. As sections 5.1 and 5.2 show, in a model where residual porosity

is a source of matrix buoyancy, plate spreading can initiate and maintain a component of buoyancy-driven mantle convection. In the extreme model scenario where the rate of buoyancy-driven upwelling is much larger than that caused by plate spreading, mantle convective flow is self-sustaining, and would continue even if plate spreading ceased. Furthermore, in this case, the upwelling/melting regime is a dynamic feature that is centered on the zone of greatest buoyancy, even if this is not directly beneath the ridge axis. Spatial variation of mantle temperature or composition might lead to movement of the melting regime away from its position beneath the axis.

[52] Such an extreme scenario seems unlikely for typical MORs on the Earth, but as an end-member, it provides insight into the results presented in this section. It demonstrates that convection can lead to symmetry breaking with respect to the distribution of the melting regime relative to the ridge axis. In sections 5.1 and 5.2 of the current work, and in previous work [e.g., *Scott and Stevenson, 1989*], symmetry was forced on the problem by the choice of boundary conditions. In this section I generalize the model by considering a full-ridge domain in 2-D, allowing for a linear gradient in temperature or composition at the bottom (inflow) boundary, and for ridge migration.

#### 5.3.1. Temperature Forcing

[53] A representative simulation result is shown in Figure 7 for  $U_0 = 3$  cm/yr and  $\eta_0 = 10^{18}$  Pa s. A horizontal gradient of potential temperature of 0.09 K/km is imposed at 120 km depth, on the bottom boundary. There is a temperature difference of only 3.0 K in Figure 7a from the left side (−75 km) to the right side (+40 km) of the melting region at 60 km depth. Evidently, under the conditions of this model, a small lateral temperature gradient is sufficient to cause a large asymmetry in the distribution of upwelling, melting and porosity. I quantify the extent of porosity asymmetry by defining an asymmetry parameter

$$\Psi = 2 \frac{\int_{\Omega_+} F_\phi dA}{\int_{\Omega} F_\phi dA} - 1, \quad \text{where } F_\phi = \begin{cases} 0 & \text{if } \phi = 0, \\ 1 & \text{if } \phi > 0. \end{cases} \quad (13)$$

In this equation,  $\Omega$  represents the entire domain, and  $\Omega_+$  represents the right half of the domain, where  $x > 0$ . Equation (13) states that  $\Psi = 1$  when all of the porosity is found to the right of the ridge axis,  $\Psi = 0$  when porosity is distributed evenly across the axis, and  $\Psi = -1$  when all the porosity is on the left side.

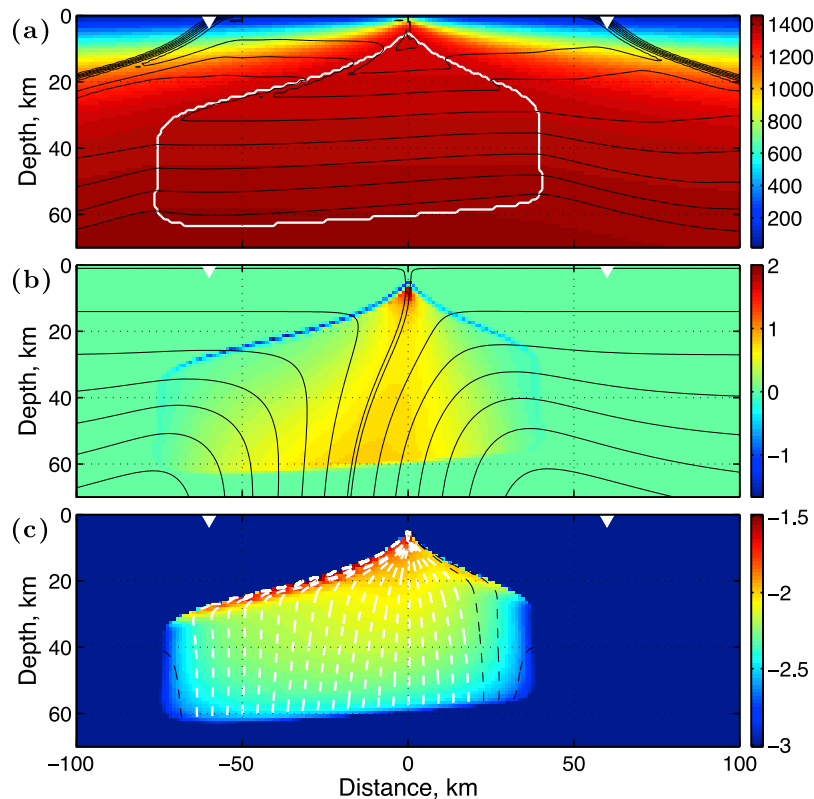


**Figure 7.** An example output at  $t = 2$  Ma showing asymmetry of the melting region arising from a gradient in mantle potential temperature of  $0.09$  K/km on the inflow (bottom) boundary. This model uses a domain size of  $400$  km width by  $120$  km depth, half-spreading rate  $U_0 = 3$  cm/yr, reference viscosities  $\eta_0 = 10^{18}$  Pa s and  $\zeta_0 = 2 \times 10^{19}$  Pa s, and mean potential temperature of  $1375^\circ\text{C}$ ; other parameters are as given in Table B2. For this calculation,  $\mathcal{V} = 105$ . (a) Temperature ( $^\circ\text{C}$ , colors), the boundary of the melting region (white line), and  $2.5\%$  contours of melt fraction (black lines). The maximum degree of melting is just above  $20\%$ . (b) The melting rate ( $\text{kg}/\text{m}^3/\text{yr}$ , colors) and mantle streamlines. (c) The  $\log_{10} \phi$  (colors) and magma streamlines. White streamlines are those focused to the ridge axis. In all three plots, white triangles are plate spreading markers that were initially at the ridge axis.

[54] Figure 8 shows how  $\Psi$  varies with spreading rate, mantle viscosity, and the magnitude of temperature gradient forcing. In Figure 8a,  $\Psi$  is plotted against the viscosity parameter  $\eta_0$ ; curves for different spreading rates are nearly superimposed on each other. Figure 8b shows  $\Psi$  plotted against the predicted ratio of maximum upwelling rate to that expected for passive spreading. In contrast to Figure 8a, lines representing different spreading rates can be clearly distinguished. Although the data is sparse, there is a roughly linear relation between the vigor of active convection and the degree of asymmetry. The slope of this line increases with spreading rate. Further consideration of this observation is given in section 6.

### 5.3.2. Compositional Forcing

[55] Mantle heterogeneity in the Earth is composed of spatial variation in both temperature and com-

position. Figure 9a shows how  $\Psi$  varies with mantle viscosity and the magnitude of composition gradient forcing  $dC_m/dx$ . This gradient is imposed on the domain's bottom boundary, so that inflowing mantle has composition  $C_0$  at the center of the domain, and deviates from this with distance from that point according to  $x dC_m/dx$ . For reasons that are not well understood, these model calculations are more computationally challenging than the calculations for gradients in mantle temperature. The number of model runs, and the magnitude of the applied forcing, were therefore limited relative to Figure 8. It was also necessary to use a larger bulk viscosity ( $\zeta_0 = 4 \times 10^{19}$  Pa s) to obtain convergence in this case. Despite these differences, results shown in Figure 9 tell the same story as those of Figure 8: active convection beneath a mid-ocean ridge makes the upwelling and melting regime sensitive to modest asymmetry in forcing;

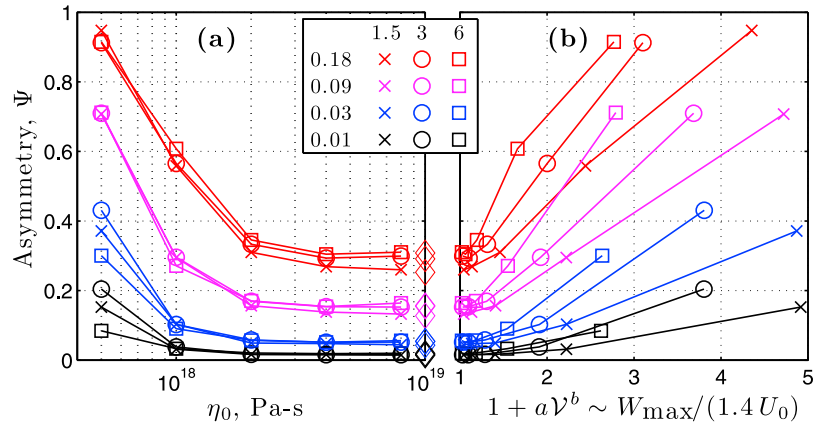


**Figure 8.** Summary of calculations with asymmetrical temperature forcing, similar to that shown in Figure 7. Each point represents a spreading rate (symbol, cm/yr) and a gradient in potential temperature along the base of the domain (color, K/km). In both plots, the calculated asymmetry  $\Psi$  is plotted on the y axis. Diamond symbols represent results from models that neglect matrix buoyancy, i.e., models of passive flow. (a) Asymmetry versus imposed viscosity parameter  $\eta_0$ . (b) Asymmetry versus the function  $1 - aV^b$ , with  $V$  defined from equation (11) and  $a, b$  constants from the best fitting line shown in Figure 3a. Smaller  $\eta_0$  corresponds to larger  $V$ .

for the same forcing, the melting regime produced under passive flow is less asymmetric.

[56] Figure 9b shows that the scaling of asymmetry  $\Psi$  is roughly linear with  $1 + aV^b$  for a fixed compositional gradient forcing, similar to the case of temperature-driven asymmetry in Figure 8b.

### 5.3.3. Ridge Migration

[57] Symmetry of sub-MOR mantle flow can also be broken by ridge migration. For a low-viscosity asthenosphere, it is reasonable to assume that mantle beneath the asthenosphere has zero hori-

zontal velocity in the hot spot reference frame [e.g., *Lenardic et al., 2006*]. Taking the frame of reference of the migrating ridge axis, the mantle flow induced by ridge migration can then be calculated by imposing the ridge migration velocity as a boundary condition on the bottom of the domain, assumed to coincide with the base of the asthenosphere. Previous work has considered the effect of ridge migration on passive mantle flow and melting in two [*Davis and Karsten, 1986; Schouten et al., 1987; Conder et al., 2002; Toomey et al., 2002; Katz et al., 2004*] and three dimensions [*Weatherley and Katz, 2010*].

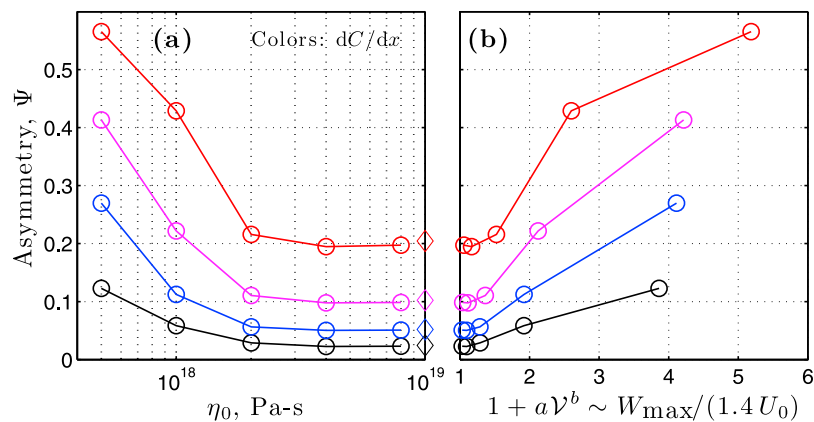


**Figure 9.** Summary of calculations with asymmetrical composition forcing. The points represent a suite of models with different values of mantle viscosity  $\eta_0$  and inflow compositional gradient  $dC_m/dx$ . Figure 9 considers only models with  $U_0 = 3$  cm/yr. Colors represent the amplitude of the gradient  $dC_m/dx$  at the inflow boundary: 0.375 (black), 0.75 (blue), 1.5 (magenta), and 3 (red)  $\times 10^{-4} \text{ km}^{-1}$ . These compositional gradients can be converted to gradients in the depth of the bottom of the melting region using equations (1a) and (2). (a) Model results plotted against  $\eta_0$ . (b) Model results plotted against  $1 + aV^b$ , as in Figure 8b.

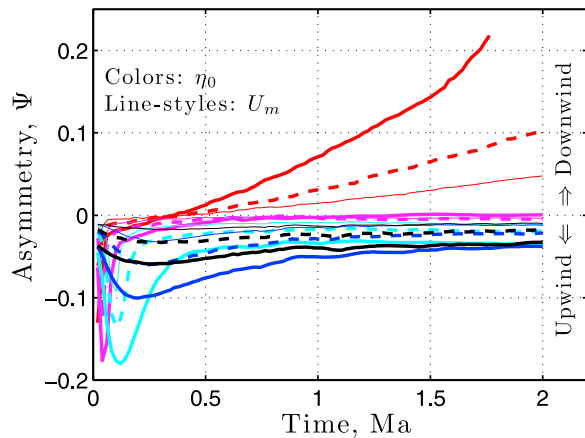


**Figure 10.** Summary of calculations with ridge migration. Asymmetry  $\Psi$  is shown as a function of time. Lines represent results from a suite of simulations with different mantle viscosity  $\eta_0$  and ridge migration rate  $U_m$ . All simulations have the same spreading rate,  $U_0 = 3$  cm/yr. Colors represent  $\eta_0$ : 0.5 (red), 1 (magenta), 2 (cyan), 4 (blue), and 8 (black)  $\times 10^{18}$  Pa s. Line styles represent  $U_m$ : 1.5 (narrow solid), 3 (dashed), and 6 (wide solid) cm/yr.

[58] Figure 10 shows the development of asymmetry of the melting region with time for a ridge that is spreading with a half rate of 3 cm/yr and migrating to the left. Results from numerical experiments for a migration rate of  $U_m = 1.5, 3, 6$  cm/yr and  $\eta_0 = 0.5, 1, 2, 4, 8 \times 10^{18}$  Pa s are plotted and show two behavioral regimes. For a more viscous mantle, ridge migration leads to enhanced melting on the leading side of the ridge (“upwind”) and a corresponding negative value of  $\Psi$ . For  $\eta_0 = 0.5 \times 10^{18}$  Pa s (red lines), ridge migration leads to positive (“downwind”) asymmetry in Figure 10. Model results shown by red lines in Figure 10 indicate that the low-viscosity runs did not reach a steady state after two million years of model time.

[59] Figure 11 gives a physical picture of the perturbation to mantle upwelling for both asymmetrical regimes. Enhanced upwelling on the upwind side of the ridge, corresponding to  $\Psi < 0$  and high  $\eta_0$  (Figure 11a), is the result of the mantle shear that arises from ridge migration; this perturbation flow must conform to the curved bottom boundary of the lithosphere [e.g., Katz et al., 2004; Conrad et al., 2010]. Enhanced upwelling on the downwind side of the ridge, corresponding to  $\Psi > 0$  and low  $\eta_0$  (Figure 11b), is the result of the convection cell that is rooted in the mantle asthenosphere and is lagging behind the leftward migrating ridge. The transition between these two regimes occurs with decreasing  $\eta_0$ : active upwelling makes an increasing contri-

bution, the melting region narrows and hence the kinematic effect of the lithospheric boundary on upwelling is diminished. At the same time, the dynamic effect of buoyancy is augmented and the ridge can move away laterally, upwind from the center of buoyancy-driven upwelling.

[60] In both classes of asymmetry development, Figure 10 shows that more rapid ridge migration relative to the half-spreading rate leads to larger  $|\Psi|$ . An assessment of global MOR data by Small and Danyushevsky [2003] indicates that the magnitude of ridge-perpendicular migration velocity clusters tightly around the half spreading rate,  $U_0$ . The magnitude of asymmetry also scales with the domain depth; work on passive flow, single-phase models demonstrates that  $|\Psi| \propto h_A^{-1}$ , where  $h_A$  is the depth of the base of the asthenosphere [Weatherley and Katz, 2010]. The domain height (and hence asthenospheric depth) for the models presented in this section and section 5 is 120 km, which is probably an underestimate by at least a factor of 2 of the actual asthenospheric thickness [e.g., Craig and McKenzie, 1986]. The magnitude of  $\Psi$  shown in Figure 10 is small relative to that arising from thermal or compositional gradients, and it would even smaller for larger  $h_A$ .

## 6. Discussion

[61] In section 3 (and in Appendix A) I presented a modified version of the two-phase, two-component model by Katz [2008] of coupled magma/mantle dynamics at mid-ocean ridges. The modifications incorporate temperature- and porosity-dependent mantle viscosity, a dike-type internal boundary for draining magma to the crust, and the capability to model buoyancy-driven mantle flow within a domain that straddles the ridge axis. A suite of half-ridge simulations performed with different model parameters was presented in section 5.1; results from these simulations were shown to be consistent with the scaling relation presented in section 4. Section 5.2 presented the dependence of crustal thickness and degree of melting on spreading rate and mantle viscosity. Section 5.3 considered asymmetrical mantle flow, melting, and porosity beneath the ridge axis. Aspects of these results are discussed in more detail below.

[62] The vigor parameter has significant predictive power in the context of the assumptions used to develop the models presented here, in particular, the assumptions of a mantle buoyancy that derives solely from the residual porosity, and a fixed den-



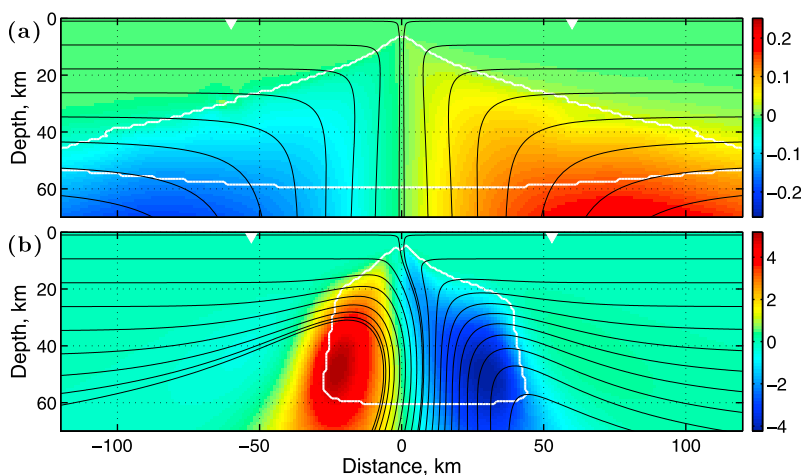


**Figure 11.** Perturbation to mantle flow arising from leftward ridge migration for two values of  $\eta_0$  at  $U_0 = 3$  cm/yr. Colors show the difference in mantle vertical velocity in cm/yr between a simulation with  $U_m = 6$  cm/yr and a simulation with  $U_m = 0$ , which are otherwise identical. Blue colors occur where upwelling is enhanced by ridge migration; red colors occur where upwelling is diminished by migration. The white contour is the outline of the melting region. Black lines are mantle streamlines of the simulations *with* ridge migration. White triangles show total spreading after  $t = 0$ . (a)  $\eta_0 = 8 \times 10^{18}$  Pa s,  $t = 2$  Ma, and  $\mathcal{V} = 13$ . This pattern of flow gives  $\Psi < 0$ . (b)  $\eta_0 = 0.5 \times 10^{18}$  Pa s,  $t = 1.77$  Ma, and  $\mathcal{V} = 253$ . This pattern of flow gives  $\Psi > 0$ . All simulations used in Figure 11 have a domain depth of 120 km.

sity difference between phases. Figure 3 shows that a simple function of  $\mathcal{V}$  can be used to reasonably estimate the contribution of buoyancy forces to upwelling, over a range of half-spreading rates. It is not surprising, then, that the same function correlates with crustal thickness and susceptibility to melting zone asymmetry. Figures 6, 8, and 9, however, show that the correlation is different for different spreading rates. This may be due to the varying shape of the lithosphere-asthenosphere boundary as a function of spreading rate. At slower spreading rates, the thermal and rheological boundary descends steeply on either side of the ridge, and laterally confines the low-viscosity region where active convection occurs. This confinement inhibits off-axis migration of the upwelling center under asymmetric buoyancy forcing, and helps explain the fanning of lines of equal forcing magnitude in Figure 8b.

[63] Nevertheless, section 5.3 shows that the amount of asymmetry developed for a given forcing is sensitive to the contribution of active convection. The maximum magnitudes of temperature and composition gradient forcing chosen for the present study are modest. In the mantle, one might expect larger gradients sustained over shorter distances; such heterogeneity is not considered here. Sharp gradients in mantle temperature were considered by *Conder et al.* [2002] and *Toomey et al.* [2002], but those studies calculated passive mantle flow only. Accounting for buoyancy forces would certainly have modified the mantle flows they computed and would have pro-

duced increased asymmetry in the melting region for equal forcing. The key question then regards the relative contribution of buoyancy-driven upwelling to MOR melting regimes.

### 6.1. Observational Constraints on Active Flow

[64] There are a variety of constraints that bear on the contribution of active flow, though none of them are conclusive. Global variation in oceanic crustal thickness is an example, and *White et al.* [2001] have produced a compilation of such data. Figure 5 shows that the data do not rule out a significant contribution from active convection. In fact, the downward trend of the data at  $U_0 > 2$  may signify a diminishing (but still important) contribution of active upwelling. The curves computed for Figure 5a derive their amplitude from a variety of ill-constrained parameters in addition to buoyancy, and thus it may be impossible to distinguish between curves on the basis of a fit to the amplitude of data. For example, past studies [e.g., *Sotin and Parmentier*, 1989] have computed crustal thickness assuming complete melt extraction from the mantle to the ridge axis. If melt focusing is inefficient, for example, or if its efficiency depends on the style of mantle flow, then the computed curves may contain a systematic offset. The present models assume values for parameters that control the focusing efficiency (especially  $\zeta_0$ ) but do not prescribe melt focusing [*Katz*, 2008].

[65] Unlike passive flow, however, active convection may yield 3-D variations in upwelling away from transform faults [Sparks and Parmentier, 1993; Jha *et al.*, 1994; Barnouin-Jha *et al.*, 1997; Choblet and Parmentier, 2001]. Observed along-axis variations in crustal thickness lead Dick *et al.* [2003] to suggest that buoyancy-driven convection is important beneath the ultraslow spreading Gakkel ridge.

[66] The predicted width of the melting regime beneath a MOR varies with the contribution of buoyancy (Figure 4). Observations of this feature are indirect, however, and highly uncertain. The MELT experiment [Forsyth *et al.*, 1998a] imaged a  $\sim 500$  km wide region of low seismic velocity that the authors attributed to the presence of mantle melt. They imaged this anomaly to extend to depths of  $\sim 150$  km, a large depth that may be indicative of the role of water in the melting regime [e.g., Asimow and Langmuir, 2003]. If a small amount of hydrous flux melting was occurring, it would explain the large width of the melting region without excluding a contribution of active upwelling near the axis. The off-axis distance of active seamounts on the Pacific plate, for example, might be another indicator of the width of the melting region. Scheirer *et al.* [1998] report that most of the recent, off-axis lava flows occur within 60 km of the axis, however on the west side of the ridge some fresh flows can be found more than 100 km away. In contrast to the MELT results, tomography of the Gulf of California [Wang *et al.*, 2009] suggests melting regions that are approximately 100 km in width.

[67] Geochemical observations may provide a means to constrain the contribution of buoyancy-driven flow to the melting regime. Figure 5b, however, shows that in the context of models reported here, active upwelling causes only a small change to the degree of melting represented by the crust, and does so only for slow to ultraslow spreading. Spiegelman [1996] showed that the distribution of trace elements transported by magma may provide a more powerful constraint. He computed two end-member, iso-viscous models, one with  $\mathcal{V} \ll 1$  (passive), and one with  $\mathcal{V} \gg 1$  (active). In the passive flow model, melt trajectories from a broad region converged to the ridge axis, delivering enriched melts there. This focusing of magmatic flow was produced by a dynamic pressure gradient [Spiegelman and McKenzie, 1987], not a sublithospheric decompression channel [Sparks and Parmentier, 1991], although the resulting melt flow trajectories are similar. The active flow calculation by Spiegelman [1996] ex-

hibited strong mantle recirculation, which injected previously depleted mantle back into the melting region (however this depleted rock was not allowed to melt). This recirculating flow regime also yielded laterally convergent streamlines of undepleted mantle just above the base of the melting region. Early melts of this undepleted source were highly enriched, while later melts, produced directly below the axis, were depleted. The magmatic streamlines of the early, enriched melts diverged away from the ridge axis, leaving only the depleted melts to arrive on axis. This combination of convergent solid flow and divergent melt flow resulted in the geochemical distinction between active and passive flow in the work of Spiegelman [1996] and Spiegelman and Reynolds [1999].

[68] Active flow models in the present work exhibit neither convergent solid flow nor divergent melt flow in the melting region. Figure 12 shows mantle streamlines and the logarithm of porosity for a simulation with  $\eta_0 = 5 \times 10^{17}$  Pa s ( $\mathcal{V} = 190$ ,  $W_{\max}/(1.4U_0) = 2.7$ ). A domain size of  $300 \times 300$  km was used for this model to minimize the influence of boundary conditions on flow in the melting region. It is evident that there is no mantle recirculation, and within the melting region there is no lateral convergence of solid streamlines. This difference from the active flow end-member of Spiegelman [1996] may be attributable to the larger domain size and the  $T$ -dependent viscosity that yields a rigid lithosphere. Magmatic streamlines (not shown in Figure 12) are focused to the ridge axis. One might therefore expect, in contrast to the prediction of Spiegelman [1996], that the trace element enrichment of on-axis lavas would not vary strongly with  $\mathcal{V}$ . Clearly this hypothesis requires further testing with calculations of trace element transport.

[69] A broad range of different observations can be applied to constrain the components of the vigor parameter  $\mathcal{V}$ . The mantle viscosity, for example, could be as large as  $10^{21}$  Pa s, according to studies of postglacial rebound [Peltier, 1998], or as low as  $5 \times 10^{17}$ , according to studies of postseismic relaxation [e.g., Panet *et al.*, 2010], or it may be both, depending on the location and time scale of the relevant flow. Constraints on mantle permeability come from experiments and models [e.g., Wark and Watson, 1998; Faul, 2001; Zhu and Hirth, 2003], as well as from inverse calculations based on geochemical transport [e.g., McKenzie, 2000; Stracke *et al.*, 2006] and magmatic flow [e.g., MacLennan *et al.*, 2002], however these different approaches yield vastly different estimates for mantle permeability. The depth of the melting region, which exerts

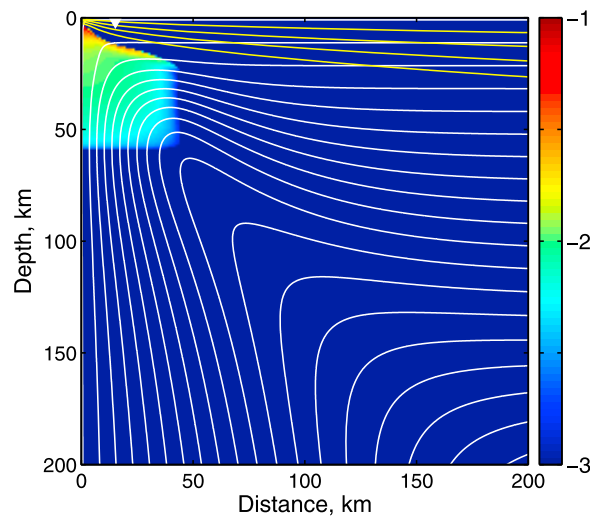


**Figure 12.** Output from a simulation with  $\eta_0 = 5 \times 10^{17}$  Pa s ( $\mathcal{V} = 190$ ) showing the absence of recirculating mantle flow. The domain size is  $300 \times 300$  km with a mesh spacing of 1 km (cropped to show  $200 \times 200$  km). The spreading rate is 4 cm/yr, and the simulation has reached a steady state. Colors represent  $\log_{10} \phi$ , from dark blue at  $\leq 0.1\%$  to red at 10% porosity; maximum porosity in the domain is 9.5%. White lines are mantle streamlines. Yellow lines are isotherms. Other parameters are as in Table B2.

an important influence on the vigor parameter, depends on the water content of the mantle [e.g., Katz *et al.*, 2003], which is thought to be about  $125 \pm 75$  ppm [e.g., Hirth and Kohlstedt, 1996]. Clearly, putting tight bounds on the value of  $\mathcal{V}$  is not yet possible.

[70] Given the considerations above, it is clear that existing constraints on mantle flow do not preclude a significant contribution of buoyancy-driven upwelling at mid-ocean ridges. A trend of slowly decreasing crustal thickness for  $U_0 > 2$  cm/yr, if it exists in the observational data, would indicate a significant role for active convection. Such a role would help to explain the asymmetry observed by seismic tomography at the MELT region of the EPR [e.g., Forsyth *et al.*, 1998a] and beneath the Gulf of California [e.g., Wang *et al.*, 2009], and would have other implications for the dynamics of a thermally and chemically heterogeneous asthenosphere.

## 6.2. Thermal and Compositional Density Variations

[71] Simulations presented here consider density variations arising only from residual porosity; previous studies have also investigated the effects of density variations arising from depletion and tem-

perature. Sotin and Parmentier [1989] considered the effect of melt depletion buoyancy beneath a ridge where the mantle surrounding the melting region was assumed to be undepleted. They concluded that depletion is a source of buoyancy driving active flow. Beneath a ridge, chemically buoyant, depleted mantle created in the melting region must spread laterally with time, however, and create a horizontal layer of depletion beneath the crust; this represents a stable stratification [Raddick *et al.*, 2002]. In a homogeneous mantle, thermal buoyancy would be unlikely to substantially modify any convective upwelling near the ridge axis. Ito *et al.* [1996] showed that for the melting region within a mantle plume, the loss of thermal buoyancy due to transfer of energy to latent heat roughly balances the gain of depletion buoyancy due to melt extraction. Farther from the ridge axis, where the thermal boundary layer has thickened substantially, thermal buoyancy may be important for triggering convective rolls aligned with the spreading direction [e.g., Barnouin-Jha *et al.*, 1997; Dumoulin *et al.*, 2008; Ballmer *et al.*, 2009].

[72] In models of a heterogeneous mantle, thermal and depletion effects on buoyancy may have greater significance. For example, the calculated asymmetry in upwelling due to imposed gradients in mantle potential temperature and composition would certainly be modified. Thermal buoyancy would reinforce the asymmetric porosity distribution, while compositional buoyancy would suppress it. This suppression would occur because fertile, denser mantle melts deeper, and to a greater extent, than depleted, less dense mantle. Such issues will be reconsidered in future work.

## 6.3. On the Absence of Porosity/Shear Bands

[73] Although it is not the main purpose of the present work, simulations described here offer an opportunity to investigate the relevance of a porosity-localizing mechanical instability beneath ridges. Experimental [e.g., Holtzman *et al.*, 2003; King *et al.*, 2010] and theoretical [e.g., Stevenson, 1989; Spiegelman, 2003; Katz *et al.*, 2006] studies have shown that partially molten mantle materials subject to shear can develop bands of locally increased porosity and deformation. These rheologically weak bands tend to emerge at a particular angle to the shear plane under simple shear deformation. Katz *et al.* [2006] proposed that they might provide a mechanism for melt focusing to the ridge axis. Butler [2009] showed that simulations that account

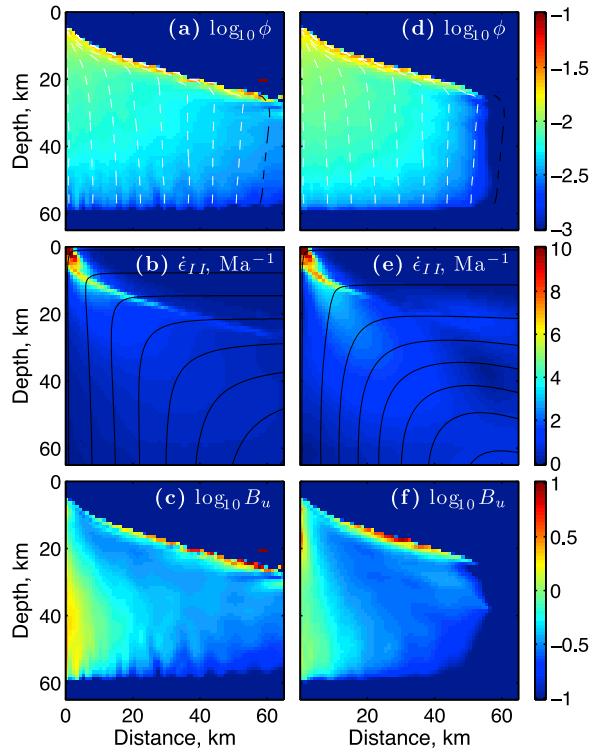


**Figure 13.** Two simulations with  $\pm 0.6\%$  white noise in the bulk composition field,  $\lambda = 90$ , and  $\zeta_0 = 10^{19}$  Pa s. Despite the exaggerated porosity weakening, no porosity/shear bands are present. (a–c)  $\eta_0 = 10^{19}$  Pa s ( $\nu = 10$ ) and (d–f)  $\eta_0 = 10^{18}$  Pa s ( $\nu = 96$ ). Figures 13a and 13d show the log of porosity in colors and magmatic streamlines. Figures 13b and 13e show the second invariant of the strain rate tensor in colors (units  $\text{Ma}^{-1}$ ) and mantle streamlines. Figures 13c and 13f show the dimensionless buoyancy to shear ratio defined by Butler [2009]. Here it is taken point-wise as  $B_u = (\Delta\rho g \delta_c) / [(\zeta + 4\eta/3)\dot{\epsilon}_{II}]$ .

for buoyancy-driven magmatic segregation in addition to large-scale mantle shear can produce porosity bands. His work demonstrated that the orientation of bands can be modified by the action of buoyancy forces; he quantified the importance of buoyancy by introducing a dimensionless ratio  $B_u = (\Delta\rho g \delta_c) / [(\zeta + 4\eta/3)\dot{\gamma}]$ .

[74] Localized bands of high porosity did not appear in the present simulations, despite inclusion of the porosity-weakening viscosity that is required to produce them. Most simulations did, of course, predict a high-porosity decompaction channel at the base of the lithosphere, but this feature is independent of the mechanical instability associated with porosity bands [Sparks and Parmentier, 1991]. Emergence of porosity bands in simulations of experimental conditions by Katz et al.

[2006] were sensitive to the amplitude of the initial noise that was introduced; simulations described above contained no initial noise. To test the importance of initial noise for porosity band emergence in MOR models, I ran the two simulations shown in Figure 13. These two runs (for  $\eta_0 = 10^{19}$  Pa s and  $10^{18}$  Pa s) started with an initial noise in the bulk composition of  $\pm 0.6\%$  of  $C_0$ . They were run with enhanced porosity weakening:  $\lambda = 90$  in equation (3), rather than the usual value of 27.

[75] The compaction length in the center of the melting region of Figure 13 is  $\sim 15$  km, and so it is well resolved by the 1 km grid spacing. Various studies have shown that the spacing of porosity bands arising from mechanical instability is expected to be less than or equal to the compaction length [e.g., Spiegelman, 2003]. Numerical models performed by Katz et al. [2006] suggest that within this range, it is the wavenumber spectrum of initial noise that controls the spacing of bands. The simulations presented in Figure 13 use an initial noise field with spectral power at scales smaller than the compaction length, and hence should enable growth of porosity bands at that scale.

[76] Variations in the porosity field in Figures 13a and 13d indicate the presence of compositional heterogeneity, but no shear bands are evident after two million years of simulated time. The second invariant of the strain rate tensor, shown in Figures 13b and 13e, is enhanced along the decompaction channel at the base of the lithosphere, but is otherwise smooth. Figures 13c and 13f show the point-wise value of  $\log_{10} B_u$ . The size of this parameter within the melting region is small relative to the prediction of Butler [2009, Figure 1]. According to his analysis, at small values of  $B_u$ , buoyancy does not affect the orientation of shear bands.

[77] Porosity band emergence and orientation was considered by Takei and Holtzman [2009c], who introduced an anisotropic viscosity tensor based on the homogenized contiguity between mantle grains. Their work predicted larger growth rates of instabilities than did Katz et al. [2006], and obtained band orientations consistent with experiments [Holtzman et al., 2003] without invoking non-Newtonian viscosity. It is possible that their proposed rheology and/or a non-Newtonian viscosity, and/or a much lower value of  $\zeta_0$  would give a different result in terms of mechanical instability and the emergence of porosity bands. A network of high-permeability melt channels, regardless of their

origin, might change the melt retention properties of the melting region and hence affect the vigor of active convection, relative to diffuse porous flow.

#### 6.4. Toward Models of 3-D Magma/Mantle Flow and Ridge Relocation

[78] Much past work, and in particular that of *Barnouin-Jha et al.* [1997] and *Choblet and Parmentier* [2001], showed that active flow can lead to three-dimensional upwelling and melting structure beneath an idealized MOR without ridge offsets. The natural ridge system, of course, imposes a 3-D structure on asthenospheric flow due to the presence of transform faults [*Dumoulin et al.*, 2008], overlapping spreading centers, and other forms of offset. These offsets are associated with asymmetries in ridge properties [*Carbotte et al.*, 2004] that are indicative of complexity in the mantle flow and melting regime beneath. Present two-phase models have not been extended to three dimensions, though this is a goal for future work. Significant 3-D structure is expected based on past work with numerical models by other authors, and is consistent with seismic tomography [e.g., *Wang et al.*, 2009]. Most models, however, have not explicitly incorporated magmatic flow. While this omission reduces computational cost and complexity, it precludes the models from addressing questions of 3-D magmatic transport near ridge offsets, and along ridge segments. A 3-D extension of present models will be a powerful tool for investigating these dynamics.

[79] *Mittelstaedt et al.* [2008] investigated the interaction of a mantle plume with a MOR and showed that thermomagmatic erosion of the lithosphere by plume-derived magma can produce dynamic relocation of the ridge axis. Key to this process is the transport and deposition of latent heat by magma. Two-phase models can quantify this heat transport and model thermomagmatic erosion of the lithosphere. Combining dynamic ridge relocation [e.g., *Gerya*, 2010] with three dimensional models of coupled magma/mantle dynamics will enable a study of how magmatism affects the morphological evolution of the MOR system. In particular, it will be possible to investigate the influence of an asymmetric melting region on the location and kinematics of the ridge axis.

### 7. Summary

[80] In the present article I introduced a modified version of the two-dimensional, two-phase, two-component model of magma/mantle interaction

beneath mid-ocean ridges developed by *Katz* [2008]. The thermodynamics of the system are captured with the Enthalpy Method, and with a simple, binary phase diagram. The components are not actual chemical species, but instead represent “enriched” and “depleted” end-members in a one dimensional composition space. The fluid mechanics of the system are governed by a set of equations derived by *McKenzie* [1984] and reconsidered by many other authors.

[81] The inclusion of constitutive laws controlling the temperature and porosity dependence of mantle rheology allowed simulations to capture the rigid oceanic lithosphere. The equations account for buoyancy forces that arise from the presence of a less dense magma in the pores of the mantle matrix.

[82] I obtained numerical solutions to the governing equations in domains that are oriented vertically, perpendicular to the ridge axis. Some solutions were computed on half-ridge domains, while others were computed in domains that straddle the ridge axis. Solutions were analyzed to understand the characteristics and consequences of buoyancy-driven mantle flow on the mid-ocean ridge melting regime. In particular, motivated by observations of asymmetric seismic wave speed distributions in tomographic surveys of the subridge asthenosphere, I investigated the development of asymmetric upwelling and melting in the presence of buoyancy-driven mantle flow.

[83] The key findings of this study are as follows:

[84] 1. The effect of buoyancy due to residual porosity on the flow and melting regime beneath MORs (i.e., the *vigor* of active convection) can be characterized by a simple function of a nondimensional parameter that is analogous to the Rayleigh number.

[85] 2. The width of the melting region is a decreasing function of convective vigor. Crustal thickness increases linearly with vigor, while the degree of melting inferred from the composition of the crust is independent of vigor.

[86] 3. The response of the system to an asymmetric forcing (e.g., ridge migration or a gradient in mantle potential temperature or composition) is amplified when buoyancy forces are important. Even under vigorous convection, however, ridge migration has a smaller effect than asymmetric thermal or compositional gradients.

[87] 4. Although the viscosity law used in simulations provides the necessary conditions for mechan-

ical instability and emergence of porosity/shear bands, this instability was not observed to occur. Even tests with compositional noise and enhanced porosity weakening did not exhibit the emergence of porosity/shear bands.

[88] The current models are based on simplifications that limit a quantitative mapping between results obtained here and observations of natural systems. First, convection is an inherently three dimensional process; 2-D models of convection cannot properly capture the scaling properties of the real system. Second, current models neglect thermal and compositional density variation. And finally, the symmetry-breaking thermal and compositional gradients are a highly idealized representation of mantle heterogeneity. Despite these limitations, the results presented here indicate that buoyancy-driven mantle flow increases the sensitivity of the MOR melting regime to the development of asymmetry, and may help to explain the unexpectedly asymmetric wave speed distributions in the subridge asthenosphere, as observed by seismic tomography.

## Appendix A: Governing Equations

[89] The equations used in the present work to model the fluid mechanics of coupled magma/mantle flow are well established. Their first derivation was by *McKenzie* [1984] but other authors have derived equivalent or more general versions [*Fowler*, 1985; *Ribe*, 1985b; *Scott and Stevenson*, 1986; *Spiegelman*, 1993; *Bercovici et al.*, 2001]. *Katz et al.* [2007] introduced a pressure decomposition and reformulated the equations in a manner that is well suited to numerical solution; this decomposition is used in the present work. *McKenzie* [1984] derived a statement of conservation of energy for the two-phase system and recent work has clarified, extended, and developed solutions for this equation [e.g., *Šrámek et al.*, 2007; *Hewitt and Fowler*, 2008].

[90] The equations and numerical approach used here are related to the work of all of these authors, but are most closely based on *Katz* [2008]. In fact, the differences between that work and the current modeling approach are small. They are (1) inclusion of buoyancy terms in the governing equations, (2) consideration of the temperature dependence of bulk and shear viscosity and the porosity dependence of shear viscosity, and (3) linearization of the petrological phase boundaries used as closure conditions for the Enthalpy Method. Like

the model proposed by *Katz* [2008], the current simulations use a two-component thermodynamic system, assume thermodynamic equilibrium, and apply the Enthalpy Method to derive closure conditions.

### A1. Conservation of Mass and Momentum

[91] To expose these differences and for clarity of presentation, I review the full set of conservation equations and constitutive laws below. I begin with the conservation of mass and momentum equations derived by *McKenzie* [1984]:

$$\frac{\partial \rho_f \phi}{\partial t} + \nabla \cdot \rho_f \phi \mathbf{v}_f = \Gamma, \quad (\text{A1a})$$

$$\frac{\partial \rho_m (1 - \phi)}{\partial t} + \nabla \cdot \rho_m (1 - \phi) \mathbf{v}_m = -\Gamma, \quad (\text{A1b})$$

$$\phi (\mathbf{v}_f - \mathbf{v}_m) = -\frac{K}{\mu} [\nabla P_f - \rho_f \mathbf{g}], \quad (\text{A1c})$$

$$\nabla P_f = \nabla \cdot [\eta (\nabla \mathbf{v}_m + \nabla \mathbf{v}_m^T)] + \nabla \cdot \left[ \left( \zeta - \frac{2}{3} \eta \right) \nabla \cdot \mathbf{v}_m \right] + \bar{\rho} \mathbf{g}, \quad (\text{A1d})$$

where subscripts  $f$  and  $m$  represent the fluid and matrix phases, respectively.  $\rho$  is density;  $\phi$  is the porosity or volume fraction of fluid phase;  $\mathbf{v}$  is velocity;  $\Gamma$  is the mass transfer rate between phases (e.g., melting);  $P_f$  is the fluid pressure;  $K$  is the permeability; and  $\mu$ ,  $\eta$ , and  $\zeta$  are the fluid, matrix shear, and matrix bulk viscosities, respectively;  $\mathbf{g}$  is the gravity vector. For any variable or product of variables,  $Q$ , defined for each phase,  $\bar{Q} = \phi Q_f + (1 - \phi) Q_m$ . The first two equations represent conservation of mass for each phase, the second two equations represent force balance for each phase. For further details, see any of the references above.

### A2. Phase Densities, Pressure Decomposition, and Reformulation

[92] To account for variations in density due to temperature and composition, I introduce linearized expressions for the densities

$$\rho_m = \rho_{m0} (1 - B_m), \quad (\text{A2a})$$

$$\rho_f = \rho_{f0} (1 - B_f) \quad (\text{A2b})$$

$$\text{with } B_i = \alpha (T - T_0) + \beta (C_i - C_0), \quad (\text{A2c})$$

where  $\alpha$  and  $\beta$  are the coefficients of thermal and compositional expansion, respectively;  $T$  is the temperature;  $C$  is the concentration of the less dense and less fusible component; and the subscript  $i$  is replaced with either the fluid  $f$  or matrix  $m$  phase. The constants  $\rho_{f0}$ ,  $\rho_{m0}$ ,  $T_0$ , and  $C_0$  are reference values.  $B$  can be thought of as the relative buoyancy of each phase. Below I make the Boussinesq approximation, taking  $\rho_f = \rho_m = \rho$  as a constant in all nonbuoyancy terms.

[93] Following *Katz et al.* [2007], I decompose pressure into three parts

$$P_f = P_l + \mathcal{P} + P \quad (\text{A3})$$

where  $P_l = \rho_{m0}gz$  is the reference lithostatic pressure,  $\mathcal{P} = (\zeta - 2\eta/3)\nabla \cdot \mathbf{v}_m$  is the compaction pressure, and  $P$  is the dynamic pressure.

[94] Using equations (A2) and (A3) and applying the Boussinesq approximation, I reformulate the conservation equations (A1c) and (A1d) as

$$-\nabla \cdot \frac{K}{\mu} \nabla \mathcal{P} + \frac{\mathcal{P}}{\xi} = \nabla \cdot \frac{K}{\mu} [\nabla P + (\Delta\rho + \rho_{f0}B_f)\mathbf{g}], \quad (\text{A4a})$$

$$\nabla P = \nabla \cdot \eta (\nabla \mathbf{v}_m + \nabla \mathbf{v}_m^T) - (\phi\Delta\rho + \overline{\rho_0 B})\mathbf{g}, \quad (\text{A4b})$$

where  $\xi = (\zeta - 2\eta/3)$  and  $\Delta\rho = \rho_{m0} - \rho_{f0}$ . The first of this set is the Compaction equation, governing volumetric deformation of the matrix; the second is the Stokes equation.

[95] In addition to the model for density variations in (A2), the system of equations requires closure relations in the form of constitutive laws for permeability, shear viscosity, and bulk viscosity. These were presented in the main text, above, and are not repeated here.

### A3. Conservation of Energy and Species Mass

[96] Following [*Katz*, 2008], conservation of energy is cast as an equation for enthalpy  $\mathcal{H}$

$$\frac{\partial \mathcal{H}}{\partial t} + \rho c_P \mathbf{e}^{\frac{\alpha \xi}{c_P}} \nabla \cdot \bar{\mathbf{v}} T = L\rho \nabla \cdot (1 - \phi)\mathbf{v}_m + k \mathbf{e}^{\frac{\alpha \xi}{c_P}} \nabla^2 T, \quad (\text{A5})$$

where  $c_P$  is the specific heat capacity,  $T$  is the potential temperature in Kelvin,  $L$  is the latent heat per kilogram, and  $k$  is the thermal conductivity (assumed equal between phases). This equation

states that changes in enthalpy at a point are due to advection of sensible heat, advection of latent heat, and thermal diffusion. The conservation of bulk species mass used by *Katz* [2008] is

$$\frac{\partial C}{\partial t} + \nabla \cdot \phi \mathbf{v}_f C_f + \nabla \cdot (1 - \phi)\mathbf{v}_m C_m = \mathcal{D} \nabla \cdot \phi \nabla C_f, \quad (\text{A6})$$

where  $\mathcal{D}$  is the chemical diffusivity. This equation states that changes in bulk composition are due to advection by each phase and diffusion through the fluid phase.

[97] Equations (A5) and (A6) contain variables  $T$ ,  $\phi$ ,  $C_m$ , and  $C_f$ . Closure requires that I express the four variables as functions of the enthalpy  $\mathcal{H}$  and bulk composition  $C$ . *Katz* [2008] showed that the Enthalpy Method [*Alexiades and Solomon*, 1993] is suited for this task. Assuming thermal equilibrium in a two-phase, two-component system and neglecting variations in partial specific entropy, I write the following four equations:

$$\mathcal{H} = \rho L \phi + \rho c_P (T - T_0). \quad (\text{A7a})$$

$$C = \phi C_f + (1 - \phi) C_m, \quad (\text{A7b})$$

$$C_S = f_S(T, P_f), \quad (\text{A7c})$$

$$C_L = f_L(T, P_f). \quad (\text{A7d})$$

The first of these is the definition of bulk enthalpy, and says that the enthalpy equals the sum of the latent and sensible energy; the second is the definition of bulk composition; the third and fourth are the solidus and liquidus equations, respectively, that specify the composition of the coexisting solid and liquid phase in equilibrium at a given pressure and temperature. These can be combined to give an equation for the porosity,

$$\phi f_L \left( \frac{\mathcal{H} - \rho L \phi}{\rho c_P} + T_0, P_f \right) + (1 - \phi) f_S \left( \frac{\mathcal{H} - \rho L \phi}{\rho c_P} + T_0, P_f \right) - C = 0. \quad (\text{A8})$$

The solution of (A8) can be substituted back into (A7a) to obtain  $T$ , which can then be used to compute the phase compositions from (A7c) and (A7d). *Katz* [2008] generalized this method to two-

**Table A1.** A Summary of Nondimensional Parameters<sup>a</sup>

Parameter	Typical Size	Comment
$\delta = \frac{1}{H} \left( \frac{K_0 \eta_0}{\mu} \right)^{1/2}$	3	Compaction length
$\alpha^* = \frac{\rho \alpha \Delta T}{\Delta \rho}$	$7 \times 10^{-3}$	Thermal expansivity
$\beta^* = \frac{\rho \beta \Delta C}{\Delta \rho}$	0	Compositional expansivity
$\mathcal{A} = \frac{H \alpha g}{c_p}$	0.03	Adiabatic parameter
$\mathcal{S} = \frac{L}{c_p \Delta T}$	8	Stefan number
$\text{Pe}_T = \frac{H w_0}{\kappa}$	$6 \times 10^7$	Thermal Peclet number
$\text{Pe}_C = \frac{H w_0}{D}$	$6 \times 10^9$	Compositional Peclet number
$G = \frac{H \Delta \rho g}{\gamma \Delta T}$	$9 \times 10^8$	Inverse Clapeyron slope
$R_M = \frac{M_S}{M_L}$	1	Ratio of solidus to liquidus slope

<sup>a</sup>Typical sizes are calculated using a domain height  $H = 120$  km. These parameters are for nondimensionalization of the problem and are not necessarily indicative of physical balances of terms in the governing equations.

phase systems with more than two components; I do not pursue that extension here.

#### A4. Nondimensionalization

[98] To nondimensionalize the above equations, I employ the following variables

$$\theta = \frac{T - T_0}{\Delta T}, \quad \tilde{\theta} = \frac{T - T_0}{\Delta T}, \quad \Theta = \frac{C - C_0}{\Delta C}, \quad (\text{A9})$$

where  $\Delta T = M_S \Delta C$  (the definitions of  $M_S$  and  $\Delta C$  are given in section 3.1). I also define the following characteristic scales

$$\begin{aligned} x &= Hx', & \mathbf{v} &= w_0 \mathbf{v}', & t &= \frac{H}{w_0} t', \\ K &= K_0 K', & P &= H \Delta \rho_0 g P', & \mathcal{H} &= \rho c_p \Delta T \mathcal{H}', \\ (\eta, \zeta, \xi) &= \eta_0 (\eta', \zeta', \xi'), & (\Gamma, S) &= \frac{w_0 \rho}{H} (\Gamma', S') & w_0 &= \frac{K_0 \Delta \rho_0 g}{\mu}, \end{aligned}$$

where  $H$  is a characteristic domain size,  $w_0$  is a characteristic Darcian fluid velocity,  $K_0$  is a proportionality constant for permeability (that should vary with grain size, dihedral angle, etc. but is held constant here for simplicity), and  $\eta_0$  is a reference value for viscosity.

[99] Using these scales, dropping primes and rearranging gives

$$\nabla P = \delta^2 \nabla \cdot \eta (\nabla \mathbf{v}_m + \nabla \mathbf{v}_m^T) - (\phi + \mathcal{B}) \hat{\mathbf{g}}, \quad (\text{A10a})$$

$$\nabla \cdot \mathbf{v}_m = \nabla \cdot K [\nabla P + \nabla \mathcal{P} + (1 + \mathcal{B}_f) \hat{\mathbf{g}}], \quad (\text{A10b})$$

$$\mathcal{P} = \delta^2 \xi \nabla \cdot \mathbf{v}_m, \quad (\text{A10c})$$

$$\partial_t \mathcal{H} + e^{A_z} \nabla \cdot \bar{\mathbf{v}} \theta = \mathcal{S} \nabla \cdot (1 - \phi) \mathbf{v}_m + e^{A_z} \text{Pe}_T^{-1} \nabla^2 \theta, \quad (\text{A10d})$$

$$\partial_t \Theta + \nabla \cdot \phi \mathbf{v}_f \Theta_f + \nabla \cdot (1 - \phi) \mathbf{v}_m \Theta_m = \text{Pe}_C^{-1} \nabla \cdot \phi \nabla \Theta_f, \quad (\text{A10e})$$

where  $\hat{\mathbf{g}} = \mathbf{g}/|\mathbf{g}|$  is a unit vector pointing in the direction of gravity and

$$\mathcal{B}_f = \alpha^* \theta + \beta^* \Theta_f, \quad (\text{A11a})$$

$$\mathcal{B} = \alpha^* \theta + \beta^* \Theta \quad (\text{A11b})$$

are dimensionless buoyancy parameters. This set of equations contains nondimensional ratios  $\delta$ ,  $\alpha^*$ ,  $\beta^*$ ,  $\mathcal{A}$ ,  $\mathcal{S}$ ,  $\text{Pe}_T$ , and  $\text{Pe}_C$ ; these are defined and explained in Table A1.

[100] The linearized equations for the solidus (1a) and liquidus (1b) are nondimensionalized according the same scheme and become

$$\Theta_S = \tilde{\theta}_S - P_f G, \quad (\text{A12a})$$

$$\Theta_L = R_M (\tilde{\theta}_L - P_f G) - 1, \quad (\text{A12b})$$

where  $P_f$  is the nondimensional pressure,  $G$  is a nondimensional inverse Clapeyron slope, and  $R_M$  is the ratio of solidus to liquidus slope (see Table A1).

[101] Using (A12a) and (A12b) with nondimensionalized definitions of bulk enthalpy and composition, equation (A8) can be rewritten in nondimensional form as

$$\Theta + \phi - [1 + \phi(R_M - 1)](\mathcal{H} - \mathcal{S}\phi - P_f G) = 0, \quad (\text{A13})$$

which is a quadratic equation that can be solved for the porosity as a function of enthalpy and bulk composition,  $\phi = \phi(\mathcal{H}, \Theta)$ .

#### A5. Numerical Solution

[102] The governing equations (A10) and constitutive laws are discretized using a finite volume scheme on a staggered mesh with  $1 \times 1$  km cell size. At each time step, the full system of implicit, nonlinear algebraic equations is separated into two parts that are solved iteratively. The first part comprises equations governing the mechanics (A10a)–(A10c), while the second part is built from the equations governing thermochemistry, (A10d) and (A10e). Each block of equations is solved in the PETSc framework using an Incomplete LU pre-



**Table B1.** Model Runs, Parameters, and Results Used in Figure 3<sup>a</sup>

Run ID	$U_0$ (cm/yr)	$\eta_0$ ( $10^{18}$ Pa s)	$K_0$ ( $10^{-7}$ m <sup>2</sup> )	$\Delta\rho$ (kg/m <sup>3</sup> )	$f$	$\mathcal{V}$	$\mathcal{V}_W$	$W_{\max}/(1.4U_0)$
mr5674	1.5	0.125	1	500	0.1	1062.02	3418.70	23.83
mr6020	1.5	0.2	1	500	0.1	635.98	1764.70	15.26
mr5659	1.5	0.25	1	500	0.1	505.88	1306.09	12.29
mr5675	1.5	0.35	1	500	0.1	358.70	805.40	8.09
mr5658	1.5	0.5	1	500	0.1	239.30	466.25	5.28
mr5655	1.5	1	1	500	0.1	114.06	173.10	2.50
mr5660	1.5	1	0.1	500	0.1	281.41	553.30	5.43
mr5656	1.5	2	1	500	0.1	56.88	73.15	1.52
mr5661	1.5	2	0.1	500	0.1	134.17	199.44	2.35
mr5657	1.5	4	1	500	0.1	28.39	34.19	1.25
mr5662	1.5	4	0.1	500	0.1	64.04	81.93	1.50
mr5663	1.5	8	0.1	500	0.1	31.95	38.37	1.24
mr5665	1.5	100	1	500	0.1	1.13	1.29	1.07
mr5681	1.5	1000	1	500	0.1	0.11	0.13	1.04
mr5643	3	0.25	10	500	0.1	186.07	312.58	3.39
mr6021	3	0.3	1	500	0.1	334.79	708.67	6.77
mr5679	3	0.35	1	500	0.1	286.22	572.46	5.71
mr4741	3	0.5	1	500	0.1	200.13	351.73	3.88
mr5644	3	0.5	10	500	0.1	92.97	129.02	1.91
mr4740	3	1	1	500	0.1	99.84	139.08	1.93
mr5641	3	1	0.1	500	0.1	233.12	413.17	3.98
mr5645	3	1	10	500	0.1	44.68	54.08	1.27
mr5683	3	1	1	500	0.01	103.87	145.07	1.95
mr5684	3	1	1	500	0.1	103.60	138.86	1.72
mr5685	3	1	1	250	0.1	62.87	78.87	1.41
mr5686	3	1	1	1000	0.1	158.61	255.20	2.97
mr4739	3	2	1	500	0.1	47.93	57.97	1.26
mr5640	3	2	0.1	500	0.1	112.11	153.63	1.84
mr5636	3	4	1	500	0.1	23.91	27.49	1.09
mr5639	3	4	0.1	500	0.1	53.86	64.99	1.25
mr5637	3	8	1	500	0.1	11.91	13.50	1.04
mr5638	3	8	0.1	500	0.1	26.86	30.74	1.07
mr5666	3	100	1	500	0.1	0.95	1.07	1.02
mr5668	3	1000	1	500	0.1	0.10	0.11	1.00
mr3370	4	1	0.0625	500	0.1	236.17	422.20	4.08
mr3375	4	1	4	500	0.1	56.50	68.73	1.29
mr3491	4	1	1	500	0.1	89.73	118.07	1.63
mr3492	4	1	0.25	500	0.1	147.92	219.74	2.34
mr3494	4	2	1	500	0.1	44.86	52.73	1.16
mr3495	4	2	0.25	500	0.1	73.87	91.66	1.36
mr3496	4	2	0.0625	500	0.1	117.86	160.95	1.82
mr3497	4	2	0.015625	500	0.1	197.79	363.13	4.42
mr5647	6	0.5	1	500	0.1	143.86	225.67	2.76
mr5646	6	1	1	500	0.1	71.82	91.84	1.49
mr5650	6	1	0.1	500	0.1	160.89	262.95	3.12
mr5649	6	2	0.1	500	0.1	80.36	103.38	1.52
mr5651	6	4	0.1	500	0.1	40.17	45.98	1.07
mr5653	6	8	0.1	500	0.1	20.08	22.77	1.04
mr5654	6	16	0.1	500	0.1	10.04	11.40	1.04
mr5667	6	100	1	500	0.1	0.74	0.83	0.98

<sup>a</sup>The bulk viscosity parameter  $\zeta_0 = 4 \times 10^{19}$  Pa s for all of these simulations. This value was chosen to avoid magmatic pooling along the solidus boundary, which leads to significant slowdown of the simulation code.

conditioned Newton-Krylov (Generalized Minimal Residual) method with an additive Schwartz scheme of domain decomposition. Details and references are given by *Katz et al.* [2007].

[103] The only algorithmic difference from the approach presented by *Katz et al.* [2007] is that the

current simulations are accelerated with staggered time stepping. Thermochemical variables  $\mathcal{H}$  and  $\Theta$  (along with  $\phi$ ,  $\theta$ ,  $\Theta_m$  and  $\Theta_f$ ) are updated at each time step,  $\Delta t$ . Also, the compaction equation (A10b) is solved at each time step. The computationally expensive Stokes equation (A10a) and associated

**Table B2.** Dimensional Parameters Used in the Model and Their Preferred Values

Quantity	Symbol	Definition	Range Considered	Preferred Value	Units
Half-spreading rate	$U_0$		0.5–7	3	cm/yr
Ridge migration rate	$U_m$		0.5–7	$U_0$	cm/yr
Permeability const.	$K_0$	$K = K_0\phi^n$	$10^{-8}$ – $10^{-6}$	$10^{-7}$	$m^2$
Permeability exponent	$n$	ibid		3	
Mantle shear visc. const.	$\eta_0$	equation (3)	$5 \times 10^{17}$ – $8 \times 10^{19}$	$10^{18}$	Pa s
Reference viscous temp.	$T_{\eta_0}$	equation (3)		see note <sup>a</sup>	°C
Activation energy	$E^*$	equation (3)		$3 \times 10^5$	J mol <sup>-1</sup>
Viscosity constant	$\lambda$	equation (3)		27	
Mantle bulk visc. const.	$\zeta_0$	equation (4)	$10^{18}$ – $4 \times 10^{19}$	$2 \times 10^{19}$	Pa s
Magma viscosity	$\mu$			1	Pa s
Boussinesq density	$\rho$			3000	kg m <sup>-3</sup>
Boussinesq density diff.	$\Delta\rho$			500	kg m <sup>-3</sup>
Spec. heat capacity	$c_p$			1200	J kg <sup>-1</sup> K <sup>-1</sup>
Thermal diffusivity	$\kappa$			$10^{-6}$	m <sup>2</sup> s <sup>-1</sup>
Coef. thermal exp. <sup>b</sup>	$\alpha$			$3 \times 10^{-5}$	K <sup>-1</sup>
Latent heat	$L$			$4 \times 10^5$	J kg <sup>-1</sup>
Chemical diffusivity	$\mathcal{D}$			$10^{-8}$	m <sup>2</sup> s <sup>-1</sup>
Potential temperature	$\mathcal{T}_m$			1375	°C
Reference melting temp.	$T_0$	equation (1)		1292	°C
Clapeyron slope	$\gamma$	equation (1)		$60^{-1}$	GPa K <sup>-1</sup>
Composition diff.	$\Delta C$	equation (1)		0.1	wt frac.
Solidus, liquidus slope	$M_S, M_L$	equation (1)		400	K (wt frac.) <sup>-1</sup>
Dike underpressure coef.	$\mathcal{F}$	equation (5)	0.001–0.1	0.005	

<sup>a</sup>The value of this parameter is chosen such that  $\eta = \eta_0$  for potential temperature  $\mathcal{T}_m$ , composition  $C_0$ , and zero porosity, at the depth given by equation (2).

<sup>b</sup>The coefficient of thermal expansion is used to calculate the adiabatic temperature gradient but is not used in calculating variations in density for buoyancy terms.

continuity equation (A10c) are solved at a larger time interval, however, because the tectonic-scale pattern of mantle flow evolves very slowly relative to the porosity or composition. The interval for Stokes updates is set at  $5\Delta t$  for the models described in this article. Comparison between models runs with and without staggered time stepping confirms that the loss of accuracy is insignificant at a lag of  $5\Delta t$ .

## Appendix B: Runs Used in Figure 3

[104] Table B1 gives a full list of the simulations and their parameter values that are plotted in Figure 3. Parameter values not listed in Table B1 or its caption are given in Table B2.

## Acknowledgments

[105] I am grateful to G. Ito and B. Kaus for insightful reviews, M. Spiegelman and C. Langmuir for scientific discussions, R. S. White for providing crustal thickness data, Y. Sun at the Numerical Algorithms Group for technical support, and the Oxford Supercomputing Centre and the UK National Supercomputing Service for access to well-maintained clusters. This work was supported by an academic fellowship from the Research Councils UK and by NERC grant NE/H00081X/1.

## References

- Alexiades, V., and A. D. Solomon (1993), *Mathematical Modeling of Melting and Freezing Processes*, Hemisphere, Washington, D. C.
- Asimow, P. D., and C. H. Langmuir (2003), The importance of water to oceanic mantle melting regimes, *Nature*, *421*(6925), 815–820, doi:10.1038/nature01429.
- Asimow, P. D., M. M. Hirschmann, and E. M. Stolper (1997), An analysis of variations in isentropic melt productivity, *Philos. Trans. R. Soc. London A*, *355*(1723), 255–281.
- Ballmer, M. D., J. van Hunen, G. Ito, T. A. Bianco, and P. J. Tackley (2009), Intraplate volcanism with complex age-distance patterns: A case for small-scale sublithospheric convection, *Geochem. Geophys. Geosyst.*, *10*, Q06015, doi:10.1029/2009GC002386.
- Barnouin-Jha, K., E. M. Parmentier, and D. W. Sparks (1997), Buoyant mantle upwelling and crustal production at oceanic spreading centers: On-axis segmentation and off-axis melting, *J. Geophys. Res.*, *102*(B6), 11,979–11,989.
- Batchelor, G. K. (1967), *An Introduction to Fluid Mechanics*, Cambridge Univ. Press, Cambridge, U. K.
- Bercovici, D., Y. Ricard, and G. Schubert (2001), A two-phase model for compaction and damage: 1. General theory, *J. Geophys. Res.*, *106*, 8887–8906.
- Blackman, D. K., and J. M. Kendall (1997), Sensitivity of teleseismic body waves to mineral texture and melt in the mantle beneath a mid-ocean ridge, *Philos. Trans. R. Soc. London A*, *355*(1723), 217–231.
- Bown, J. W., and R. S. White (1994), Variation with spreading rate of oceanic crustal thickness and geochemistry, *Earth Planet. Sci. Lett.*, *121*, 435–449.

- Buck, W. R., and W. S. Su (1989), Focused mantle upwelling below mid-ocean ridges due to feedback between viscosity and melting, *Geophys. Res. Lett.*, *16*(7), 641–644.
- Butler, S. L. (2009), The effects of buoyancy on shear-induced melt bands in a compacting porous medium, *Phys. Earth Planet. Inter.*, *173*(1–2), 51–59, doi:10.1016/j.pepi.2008.10.022.
- Carbotte, S. M., C. Small, and K. Donnelly (2004), The influence of ridge migration on the magmatic segmentation of mid-ocean ridges, *Nature*, *429*, 743–746.
- Choblet, G., and E. M. Parmentier (2001), Mantle upwelling and melting beneath slow spreading centers: Effects of variable rheology and melt productivity, *Earth Planet. Sci. Lett.*, *184*, 589–604.
- Conder, J. A., D. W. Forsyth, and E. M. Parmentier (2002), Asthenospheric flow and asymmetry of the East Pacific Rise, MELT area, *J. Geophys. Res.*, *107*(B12), 2344, doi:10.1029/2001JB000807.
- Conrad, C. P., B. Wu, E. I. Smith, T. A. Bianco, and A. Tibbetts (2010), Shear-driven upwelling induced by lateral viscosity variations and asthenospheric shear: A mechanism for intraplate volcanism, *Phys. Earth Planet. Inter.*, *178*(3–4), 162–175, doi:10.1016/j.pepi.2009.10.001.
- Cooper, R. F. (1990), Differential stress-induced melt migration: An experimental approach, *J. Geophys. Res.*, *95*(B5), 6979–6992.
- Craig, C. H., and D. McKenzie (1986), The existence of a thin low-viscosity layer beneath the lithosphere, *Earth Planet. Sci. Lett.*, *78*(4), 420–426.
- Davis, E. E., and J. L. Karsten (1986), On the cause of the asymmetric distribution of seamounts about the Juan De Fuca ridge—Ridge-crest migration over a heterogeneous asthenosphere, *Earth Planet. Sci. Lett.*, *79*(3–4), 385–396.
- Dick, H. J. B., J. Lin, and H. Schouten (2003), An ultraslow-spreading class of ocean ridge, *Nature*, *426*(6965), 405–412, doi:10.1038/nature02128.
- Dumoulin, C., G. Choblet, and M. P. Doin (2008), Convective interactions between oceanic lithosphere and asthenosphere: Influence of a transform fault, *Earth Planet. Sci. Lett.*, *274*(3–4), 301–309, doi:10.1016/j.epsl.2008.07.017.
- Dunn, R. A., and D. W. Forsyth (2003), Imaging the transition between the region of mantle melt generation and the crustal magma chamber beneath the southern East Pacific Rise with short-period Love waves, *J. Geophys. Res.*, *108*(B7), 2352, doi:10.1029/2002JB002217.
- Evans, R. L., P. Tarits, A. D. Chave, A. White, G. Heinson, J. H. Filloux, H. Toh, N. Seama, H. Utada, J. R. Booker, and M. J. Unsworth (1999), Asymmetric electrical structure in the mantle beneath the East Pacific Rise at 17°S, *Science*, *286*(5440), 752–756.
- Faccenna, C., and T. W. Becker (2010), Shaping mobile belts by small-scale convection, *Nature*, *465*(7298), 602–605, doi:10.1038/nature09064.
- Faul, U. H. (2001), Melt retention and segregation beneath mid-ocean ridges, *Nature*, *410*, 920–923.
- Forsyth, D. W., et al. (1998a), Imaging the deep seismic structure beneath a mid-ocean ridge: The melt experiment, *Science*, *280*, 1215–1218.
- Forsyth, D. W., S. C. Webb, L. M. Dorman, and Y. Shen (1998b), Phase velocities of Rayleigh waves in the melt experiment on the East Pacific Rise, *Science*, *280*(5367), 1235–1238.
- Fowler, A. (1985), A mathematical model of magma transport in the asthenosphere, *Geophys. Astrophys. Fluid Dyn.*, *33*, 63–96.
- Gerya, T. (2010), Dynamical instability produces transform faults at mid-ocean ridges, *Science*, *329*(5995), 1047–1050, doi:10.1126/science.1191349.
- Ghods, A., and J. Arkani-Hamed (2000), Melt migration beneath mid-ocean ridges, *Geophys. J. Int.*, *140*, 687–697.
- Ghods, A., and J. Arkani-Hamed (2002), Effects of melt migration on the dynamics and melt generation of diapirs ascending through asthenosphere, *J. Geophys. Res.*, *107*(B1), 2026, doi:10.1029/2000JB000070.
- Hager, B. H., and R. J. O’Connell (1981), A simple global-model of plate dynamics and mantle convection, *J. Geophys. Res.*, *86*(B6), 4843–4867.
- Hammond, W. C., and D. R. Toomey (2003), Seismic velocity anisotropy and heterogeneity beneath the Mantle Electromagnetic and Tomography Experiment (MELT) region of the East Pacific Rise from analysis of *P* and *S* body waves, *J. Geophys. Res.*, *108*(B4), 2176, doi:10.1029/2002JB001789.
- Hernlund, J. W., D. J. Stevenson, and P. J. Tackley (2008a), Buoyant melting instabilities beneath extending lithosphere: 2. Linear analysis, *J. Geophys. Res.*, *113*, B04406, doi:10.1029/2006JB004863.
- Hernlund, J. W., P. J. Tackley, and D. J. Stevenson (2008b), Buoyant melting instabilities beneath extending lithosphere: 1. Numerical models, *J. Geophys. Res.*, *113*, B04405, doi:10.1029/2006JB004862.
- Hewitt, I. J., and A. C. Fowler (2008), Partial melting in an upwelling mantle column, *Philos. Trans. R. Soc. A*, *464*, 2467–2491, doi:10.1098/rspa.2008.0045.
- Hirth, G., and D. L. Kohlstedt (1996), Water in the oceanic upper mantle: Implications for rheology, melt extraction and the evolution of the lithosphere, *Earth Planet. Sci. Lett.*, *144*(1–2), 93–108.
- Hirth, G., and D. Kohlstedt (2003), Rheology of the upper mantle and the mantle wedge: A view from the experimentalists, in *Inside the Subduction Factory*, *Geophys. Monogr. Ser.*, vol. 138, edited by J. Eiler, pp. 83–105, AGU, Washington, D. C.
- Holtzman, B. K., N. J. Groebner, M. E. Zimmerman, S. B. Ginsberg, and D. L. Kohlstedt (2003), Stress-driven melt segregation in partially molten rocks, *Geochem. Geophys. Geosyst.*, *4*(5), 8607, doi:10.1029/2001GC000258.
- Ito, G., and R. A. Dunn (2009), Mid-ocean ridges: Mantle convection and formation of the lithosphere, in *Encyclopedia of Ocean Sciences*, edited by J. H. Steele, K. K. Turekian, and S. A. Thorpe, pp. 867–880, doi:10.1016/B978-012374473-9.00654-8, Academic, Oxford, U. K.
- Ito, G., and J. J. Mahoney (2005), Flow and melting of a heterogeneous mantle: 1. Method and importance to the geochemistry of ocean island and mid-ocean ridge basalts, *Earth Planet. Sci. Lett.*, *230*(1–2), 29–46, doi:10.1016/j.epsl.2004.10.035.
- Ito, G., J. Lin, and C. W. Gable (1996), Dynamics of mantle flow and melting at a ridge-centered hotspot: Iceland and the Mid-Atlantic Ridge, *Earth Planet. Sci. Lett.*, *144*(1–2), 53–74.
- Jha, K., E. M. Parmentier, and J. P. Morgan (1994), The role of mantle-depletion and melt-retention buoyancy in spreading-center segmentation, *Earth Planet. Sci. Lett.*, *125*(1–4), 221–234.
- Karato, S., and P. Wu (1993), Rheology of the upper mantle—A synthesis, *Science*, *260*, 771–778.
- Katz, R. F. (2008), Magma dynamics with the Enthalpy Method: Benchmark solutions and magmatic focusing at mid-ocean ridges, *J. Petrol.*, *49*, 2099–2121, doi:10.1093/ptrology/egn058.

- Katz, R. F., M. Spiegelman, and C. H. Langmuir (2003), A new parameterization of hydrous mantle melting, *Geochem. Geophys. Geosyst.*, *4*(9), 1073, doi:10.1029/2002GC000433.
- Katz, R. F., M. Spiegelman, and S. M. Carbotte (2004), Ridge migration, asthenospheric flow and the origin of magmatic segmentation in the global mid-ocean ridge system, *Geophys. Res. Lett.*, *31*, L15605, doi:10.1029/2004GL020388.
- Katz, R. F., M. Spiegelman, and B. Holtzman (2006), The dynamics of melt and shear localization in partially molten aggregates, *Nature*, *442*, 676–679, doi:10.1038/nature05039.
- Katz, R. F., M. G. Knepley, B. Smith, M. Spiegelman, and E. T. Coon (2007), Numerical simulation of geodynamic processes with the Portable Extensible Toolkit for Scientific Computation, *Phys. Earth Planet. Inter.*, *163*, 52–68, doi:10.1016/j.pepi.2007.04.016.
- King, D. S. H., M. E. Zimmerman, and D. L. Kohlstedt (2010), Stress-driven melt segregation in partially molten olivine-rich rocks deformed in torsion, *J. Petrol.*, *51*, 21–42, doi:10.1093/petrology/egp062.
- Kohlstedt, D. L., and B. K. Holtzman (2009), Shearing melt out of the Earth: An experimentalist's perspective on the influence of deformation on melt extraction, *Annu. Rev. Earth Planet. Sci.*, *37*, 561–593, doi:10.1146/annurev.earth.031208.100104.
- Lachenbruch, A. H. (1976), Dynamics of a passive spreading center, *J. Geophys. Res.*, *81*(11), 1883–1902.
- Langmuir, C. H., E. Klein, and T. Plank (1992), Petrological systematics of mid-oceanic ridge basalts: Constraints on melt generation beneath ocean ridges, in *Mantle Flow and Melt Generation at Mid-ocean Ridges*, *Geophys. Monogr. Ser.*, vol. 71, edited by J. Phipps Morgan, D. K. Blackman, and J. M. Sinton, pp. 183–280, AGU, Washington, D. C.
- Lenardic, A., M. A. Richards, and F. H. Busse (2006), Depth-dependent rheology and the horizontal length scale of mantle convection, *J. Geophys. Res.*, *111*, B07404, doi:10.1029/2005JB003639.
- MacLennan, J., M. Jull, D. McKenzie, L. Slater, and K. Grönvold (2002), The link between volcanism and deglaciation in Iceland, *Geochem. Geophys. Geosyst.*, *3*(11), 1062, doi:10.1029/2001GC000282.
- McKenzie, D. (1969), Speculations on the consequences and causes of plate motion, *Geophys. J. R. Astron. Soc.*, *18*(1), 1–32, doi:10.1111/j.1365-246X.1969.tb00259.x.
- McKenzie, D. (1984), The generation and compaction of partially molten rock, *J. Petrol.*, *25*(3), 713–765.
- McKenzie, D. (1985),  $^{230}\text{Th}$ – $^{238}\text{U}$  disequilibrium and the melting processes beneath ridge axes, *Earth Planet. Sci. Lett.*, *72*(2–3), 149–157, doi:10.1016/0012-821X(85)90001-9.
- McKenzie, D. (2000), Constraints on melt generation and transport from U-series activity ratios, *Chem. Geol.*, *162*(2), 81–94.
- McKenzie, D., and M. J. Bickle (1988), The volume and composition of melt generated by extension of the lithosphere, *J. Petrol.*, *29*(3), 625–679.
- Mittelstaedt, E., G. Ito, and M. D. Behn (2008), Mid-ocean ridge jumps associated with hotspot magmatism, *Earth Planet. Sci. Lett.*, *266*(3–4), 256–270, doi:10.1016/j.epsl.2007.10.055.
- Nicolas, A., and J. F. Violette (1982), Mantle flow at oceanic spreading centers—Models derived from ophiolites, *Tectonophysics*, *81*(3–4), 319–339.
- Panet, I., F. Pollitz, V. Mikhailov, M. Diament, P. Banerjee, and K. Grijalva (2010), Upper mantle rheology from GRACE and GPS postseismic deformation after the 2004 Sumatra-Andaman earthquake, *Geochem. Geophys. Geosyst.*, *11*, Q06008, doi:10.1029/2009GC002905.
- Parmentier, E. M., and J. Phipps Morgan (1990), Spreading rate dependence of 3-dimensional structure in oceanic spreading centers, *Nature*, *348*(6299), 325–328.
- Peltier, W. R. (1998), Postglacial variations in the level of the sea: Implications for climate dynamics and solid-earth geophysics, *Rev. Geophys.*, *36*(4), 603–689.
- Rabinowicz, M., A. Nicolas, and J. L. Vigneresse (1984), A rolling-mill effect in the asthenosphere beneath oceanic spreading centers, *Earth Planet. Sci. Lett.*, *67*, 97–108.
- Rabinowicz, M., G. Ceuleneer, and A. Nicolas (1987), Melt segregation and flow in mantle diapirs below spreading centers: Evidence from the Oman ophiolite, *J. Geophys. Res.*, *92*(B5), 3475–3486.
- Raddick, M. J., E. M. Parmentier, and D. S. Scheirer (2002), Buoyant decompression melting: A possible mechanism for intraplate volcanism, *J. Geophys. Res.*, *107*(B10), 2228, doi:10.1029/2001JB000617.
- Ribe, N. M. (1985a), The generation and composition of partial melts in the Earth's mantle, *Earth Planet. Sci. Lett.*, *73*, 361–376.
- Ribe, N. M. (1985b), The deformation and compaction of partial molten zones, *Geophys. J. R. Astron. Soc.*, *83*, 487–501.
- Rubin, K. H., and J. M. Sinton (2007), Inferences on mid-ocean ridge thermal and magmatic structure from MORB compositions, *Earth Planet. Sci. Lett.*, *260*(1–2), 257–276, doi:10.1016/j.epsl.2007.05.035.
- Scheirer, D. S., D. W. Forsyth, M. H. Cormier, and K. C. Macdonald (1998), Shipboard geophysical indications of asymmetry and melt production beneath the East Pacific Rise near the MELT experiment, *Science*, *280*(5367), 1221–1224.
- Schmeling, H. (2000), Partial melting and melt segregation in a convecting mantle, in *Physics and Chemistry of Partially Molten Rocks*, edited by N. Bagdassarov, D. Laporte, and A. B. Thompson, pp. 141–178, Kluwer Acad., Dordrecht, Netherlands.
- Schmeling, H. (2010), Dynamic models of continental rifting with melt generation, *Tectonophysics*, *480*(1–4), 33–47, doi:10.1016/j.tecto.2009.09.005.
- Schouten, H., H. J. B. Dick, and K. D. Klitgord (1987), Migration of mid-ocean ridge volcanic segments, *Nature*, *326*(6116), 835–839.
- Scott, D. R., and D. J. Stevenson (1986), Magma ascent by porous flow, *J. Geophys. Res.*, *91*, 9283–9296.
- Scott, D. R., and D. J. Stevenson (1989), A self-consistent model of melting, magma migration and buoyancy-driven circulation beneath mid-ocean ridges, *J. Geophys. Res.*, *94*, 2973–2988.
- Simpson, G., M. Spiegelman, and M. I. Weinstein (2010a), A multiscale model of partial melts: 1. Effective equations, *J. Geophys. Res.*, *115*, B04410, doi:10.1029/2009JB006375.
- Simpson, G., M. Spiegelman, and M. I. Weinstein (2010b), A multiscale model of partial melts: 2. Numerical results, *J. Geophys. Res.*, *115*, B04411, doi:10.1029/2009JB006376.
- Small, C. (1994), A global analysis of mid-ocean ridge axial topography, *Geophys. J. Int.*, *116*(1), 64–84, doi:10.1111/j.1365-246X.1994.tb02128.x.
- Small, C., and L. V. Danyushevsky (2003), Plate-kinematic explanation for mid-oceanic-ridge depth discontinuities, *Geology*, *31*(5), 399–402.
- Sotin, C., and E. M. Parmentier (1989), Dynamical consequences of compositional and thermal density stratification beneath spreading centers, *Geophys. Res. Lett.*, *16*(8), 835–838.

- Sparks, D. W., and E. M. Parmentier (1991), Melt extraction from the mantle beneath spreading centers, *Earth Planet. Sci. Lett.*, *105*(4), 368–377.
- Sparks, D. W., and E. M. Parmentier (1993), The structure of 3-dimensional convection beneath oceanic spreading centers, *Geophys. J. Int.*, *112*(1), 81–91.
- Spiegelman, M. (1993), Physics of melt extraction: Theory, implications, and applications, *Philos. Trans. R. Soc. London A*, *342*, 23–41.
- Spiegelman, M. (1996), Geochemical consequences of melt transport in 2-D: The sensitivity of trace elements to mantle dynamics, *Earth Planet. Sci. Lett.*, *139*, 115–132.
- Spiegelman, M. (2003), Linear analysis of melt band formation by simple shear, *Geochem. Geophys. Geosyst.*, *4*(9), 8615, doi:10.1029/2002GC000499.
- Spiegelman, M., and D. McKenzie (1987), Simple 2-D models for melt extraction at mid-ocean ridges and island arcs, *Earth Planet. Sci. Lett.*, *83*, 137–152.
- Spiegelman, M., and J. R. Reynolds (1999), Combined dynamic and geochemical evidence for convergent melt flow beneath the East Pacific Rise, *Nature*, *402*, 282–285.
- Šrámek, O., Y. Ricard, and D. Bercovici (2007), Simultaneous melting and compaction in deformable two-phase media, *Geophys. J. Int.*, *168*, 964–982, doi:10.1111/j.1365-246X.2006.03269.x.
- Stevenson, D. J. (1989), Spontaneous small-scale melt segregation in partial melts undergoing deformation, *Geophys. Res. Lett.*, *16*, 1067–1070.
- Stracke, A., B. Bourdon, and D. McKenzie (2006), Melt extraction in the Earth's mantle: Constraints from U-Th-Pa-Ra studies in oceanic basalts, *Earth Planet. Sci. Lett.*, *244*, 97–112, doi:10.1016/j.epsl.2006.01.057.
- Tackley, P. J., and D. J. Stevenson (1993), A mechanism for spontaneous self-perpetuating volcanism on the terrestrial planets, in *Flow and Creep in the Solar System: Observations, Modeling and Theory*, NATO ASI Ser., Ser. C, vol. 391, edited by D. B. Stone and S. K. Runcorn, pp. 307–321, Kluwer, Dordrecht, Netherlands.
- Takei, Y. (2010), Stress-induced anisotropy of partially molten rock analogue deformed under quasi-static loading test, *J. Geophys. Res.*, *115*, B03204, doi:10.1029/2009JB006568.
- Takei, Y., and B. K. Holtzman (2009a), Viscous constitutive relations of solid-liquid composites in terms of grain boundary contiguity: 1. Grain boundary diffusion control model, *J. Geophys. Res.*, *114*, B06205, doi:10.1029/2008JB005850.
- Takei, Y., and B. K. Holtzman (2009b), Viscous constitutive relations of solid-liquid composites in terms of grain boundary contiguity: 2. Compositional model for small melt fractions, *J. Geophys. Res.*, *114*, B06206, doi:10.1029/2008JB005851.
- Takei, Y., and B. K. Holtzman (2009c), Viscous constitutive relations of solid-liquid composites in terms of grain boundary contiguity: 3. Causes and consequences of viscous anisotropy, *J. Geophys. Res.*, *114*, B06207, doi:10.1029/2008JB005852.
- Toomey, D. R., W. S. D. Wilcock, S. C. Solomon, W. C. Hammond, and J. A. Orcutt (1998), Mantle seismic structure beneath the MELT region of the East Pacific Rise from P and S wave tomography, *Science*, *280*(5367), 1224–1227.
- Toomey, D. R., W. S. D. Wilcock, J. A. Conder, D. W. Forsyth, J. D. Blundy, E. M. Parmentier, and W. C. Hammond (2002), Asymmetric mantle dynamics in the MELT region of the East Pacific Rise, *Earth Planet. Sci. Lett.*, *200*(3–4), 287–295.
- Turner, J. S. (1973), *Buoyancy Effects in Fluids*, Cambridge Univ. Press, Cambridge, U. K.
- Wang, Y., D. W. Forsyth, and B. Savage (2009), Convective upwelling in the mantle beneath the Gulf of California, *Nature*, *462*(7272), 499–501, doi:10.1038/nature08552.
- Wark, D. A., and E. B. Watson (1998), Grain-scale permeabilities of texturally equilibrated, monomineralic rocks, *Earth Planet. Sci. Lett.*, *164*, 591–605.
- Weatherley, S. M., and R. F. Katz (2010), Plate-driven mantle dynamics and global patterns of mid-ocean ridge bathymetry, *Geochem. Geophys. Geosyst.*, *11*, Q10003, doi:10.1029/2010GC003192.
- White, R. S., T. A. Minshull, M. J. Bickle, and C. J. Robinson (2001), Melt generation at very slow-spreading oceanic ridges: Constraints from geochemical and geophysical data, *J. Petrol.*, *42*(6), 1171–1196.
- Wolfe, C. J., and S. C. Solomon (1998), Shear-wave splitting and implications for mantle flow beneath the MELT region of the East Pacific Rise, *Science*, *280*(5367), 1230–1232.
- Yang, Y., D. W. Forsyth, and D. S. Weeraratne (2007), Seismic attenuation near the East Pacific Rise and the origin of the low-velocity zone, *Earth Planet. Sci. Lett.*, *258*(1–2), 260–268, doi:10.1016/j.epsl.2007.03.040.
- Zhu, W. L., and G. Hirth (2003), A network model for permeability in partially molten rocks, *Earth Planet. Sci. Lett.*, *212*, 407–416.